

---

# SubsurfaceGen: Procedural Generation of Field-Scale Earth Models and Seismic Data

---

Joseph Stitt, Pratik Rathore, Madeleine Udell, Ching-Yao Lai

Stanford University

jdstitt@sep.stanford.edu, {pratikr, udell, cyaolai}@stanford.edu

🔗 **SubsurfaceGen**: <https://anonymous.4open.science/t/subsurfacegen-8961>

🔗 **Experiments**: <https://anonymous.4open.science/t/subsurfacegen-experiments-4C98>

📄 **Field-Scale Dataset**: <https://huggingface.co/datasets/subsurfacegen/field-scale-dataset>

📄 **Field-Scale Dataset (Preview)**: <https://huggingface.co/datasets/subsurfacegen/field-scale-dataset-preview>

## Abstract

Full waveform inversion (FWI) is the gold standard for subsurface imaging, with applications from carbon sequestration to energy and mineral exploration to earthquake hazard assessment. Machine learning approaches to FWI need field-scale, geologically diverse, and physically realistic training data, but existing resources such as Marmousi, SEAM, and OpenFWI fall short on spatial extent, temporal extent, geological diversity, and physical realism. We address these limitations with SubsurfaceGen, a GPU-accelerated generator for 3D velocity models and seismic data. Along with SubsurfaceGen, we release a paired dataset of 4,276 2D velocity slices, 5 s wavefields, and 8 s shot gathers drawn from 42 realistic, field-scale 3D velocity models, each spanning  $10 \text{ km} \times 10 \text{ km}$  laterally and 6.19 km deep at 10 m resolution. The dataset spans six geological settings—four built with SubsurfaceGen and two drawn from prior sources—relevant for carbon sequestration and hydrocarbon exploration. We use this dataset to evaluate neural operators on wavefield prediction and encoder–decoders on end-to-end velocity inversion, holding out one geological setting for out-of-distribution testing. These experiments surface failure modes at field-scale and demonstrate how SubsurfaceGen and the associated dataset can impact ML-based FWI.

## 1 Introduction

Subsurface imaging—the task of reconstructing the Earth’s interior from indirect surface measurements—carries significant economic and societal consequences, from verifying the integrity of carbon sequestration sites critical for addressing climate change, to discovering energy and mineral resources that underpin modern infrastructure, to assessing earthquake hazards that shape emergency planning in densely populated regions. The gold standard for subsurface imaging is full waveform inversion (FWI) [Lailly, 1983, Tarantola, 1984, Virieux and Operto, 2009], which reconstructs a *velocity model*, a spatial map of acoustic wave speed in the subsurface, from data collected in a *seismic survey*, in which an acoustic source is fired at many positions across a region of interest and an array of receivers records the reflections from the subsurface. Each source firing produces a *shot gather*: the time series recorded at the receivers in response to that firing. FWI matches these recordings to *wavefields* simulated by solving the wave equation through a candidate velocity model. However, FWI is notoriously difficult: it requires the solution of a high-dimensional, non-convex, PDE-constrained optimization problem, which suffers from cycle skipping (i.e., bad local minima) [Virieux and Operto, 2009, Yao et al., 2019], sensitivity to the initial model [Virieux and Operto, 2009], and computational costs that can scale to millions of core hours for realistic 3D surveys [Schiemenz and Igel, 2013]. Decades of research have produced sophisticated regularization schemes [Symes, 2008, Biondi and Almomin, 2014, Barnier et al., 2023] and multiscale strategies [Bunks et al., 1995, Fichtner, 2011], but the difficulties of FWI remain far from solved.

Machine learning is promising on several of these fronts. Neural operators can accelerate PDE solves in FWI, reducing overall computational costs, while maintaining accuracy and reliability [Yang et al., 2021, 2023, Zhang et al., 2023, Huang and Alkhalifah, 2025]. CNN-based encoder–decoders can directly map seismic measurements to velocity models, sidestepping the cycle skipping, initialization sensitivity, and computational costs of traditional FWI methods [Araya-Polo et al., 2018, Yang and Ma, 2019, Wu and Lin, 2020, Zhang and Lin, 2020, Farris et al., 2023, Wang et al., 2023b]. Generative models can learn data-driven regularizers from existing velocity models, capturing realistic geological features that classical regularizers like Tikhonov and total variation are unable to represent [Mosser et al., 2020, Stitt et al., 2023, Wang et al., 2023a, Stitt et al., 2025].

However, progress on these fronts is bottlenecked by data. The velocity models used to train and evaluate ML-based FWI should resemble the surveys they will be deployed on—*field-scale*, geologically diverse, and physically realistic—and should be extendable. By field-scale, we mean velocity models that match the geometries of real surveys: tens of kilometers laterally, several kilometers deep, with recordings over several seconds. By extendable, we mean the ability to generate new velocity models on demand. Field-scale data is necessary because cycle skipping, illumination gaps, and low-frequency recovery worsen with spatial extent, and because imaging depth scales with recording time: carbon storage and hydrocarbon reservoirs sit several kilometers below the surface, requiring recordings of 5 s or more to image. Geological diversity is needed to study generalization to unseen geologies. Physical realism guards against ML methods producing nonsensical geological features. Extendability supports studying scaling behavior, distribution shift, and generalization across new geological settings.

Popular datasets for FWI, such as Marmousi [Versteeg, 1994, Martin et al., 2006], SEAM [Fehler and Kelihher, 2011], and OpenFWI [Deng et al., 2022], fall short on at least one of these criteria, whereas SubsurfaceGen, the data generator we introduce in this paper, satisfies all four (Table 1).

Table 1: SubsurfaceGen vs. existing datasets for FWI; see also Section A.1.

Resource	Field-scale?	Geologically diverse?	Physically realistic?	Extendable?
Marmousi	✓	✗	✓	✗
SEAM	✓	✗	✓	✗
OpenFWI	~	~	✗	✗
SubsurfaceGen (ours)	✓	✓	✓	✓

SubsurfaceGen is a state-of-the-art data generator that enables procedural generation of field-scale, geologically diverse, physically realistic 3D velocity models and seismic data. Our contributions (illustrated in Fig. 1) are as follows:

- **Realistic velocity model generation (Section 3).** SubsurfaceGen allows users to deposit geological layers with interbeds (alternating layers of contrasting velocity), and add folding, faults, salt bodies, clinofolds, and carbonate platforms, together with structure-oriented smoothing [Hale, 2009] to suppress numerical artifacts. To our knowledge, no other open-source software supports procedural generation of this range of features.
- **End-to-end seismic data generation (Section 4).** SubsurfaceGen generates shot gathers and wavefields from 2D slices of 3D velocity models using Devito [Louboutin et al., 2019], providing paired (velocity model, seismic data) samples for training and evaluation. Both velocity model and seismic data generation are GPU-accelerated, with model generation achieving up to  $26.8\times$  speedup over CPU.
- **Example 4,276 sample field-scale dataset (Sections 3.2 and 4.2).** We release a dataset on Hugging Face containing 42 field-scale 3D velocity models (each  $10\text{ km} \times 10\text{ km} \times 6.19\text{ km}$ ). From these we extract 4,276 2D slices, each paired with seismic data (5 s wavefields, 8 s shot gathers). The dataset spans six geological settings: four generated with SubsurfaceGen (based on basins in the North Sea, Gulf of Mexico, and Nova Scotia, plus a model with a large number of faults) and two drawn from prior sources (a model from a legacy 3D velocity model builder and the canonical SEAM model) to broaden geological coverage.
- **Field-scale experiments for ML-based FWI (Sections 5 and 6).** We demonstrate how SubsurfaceGen and the field-scale dataset impact ML-based FWI: for wavefield prediction, the field-scale grid forces predictions to be chunked, which motivates an adaptation of

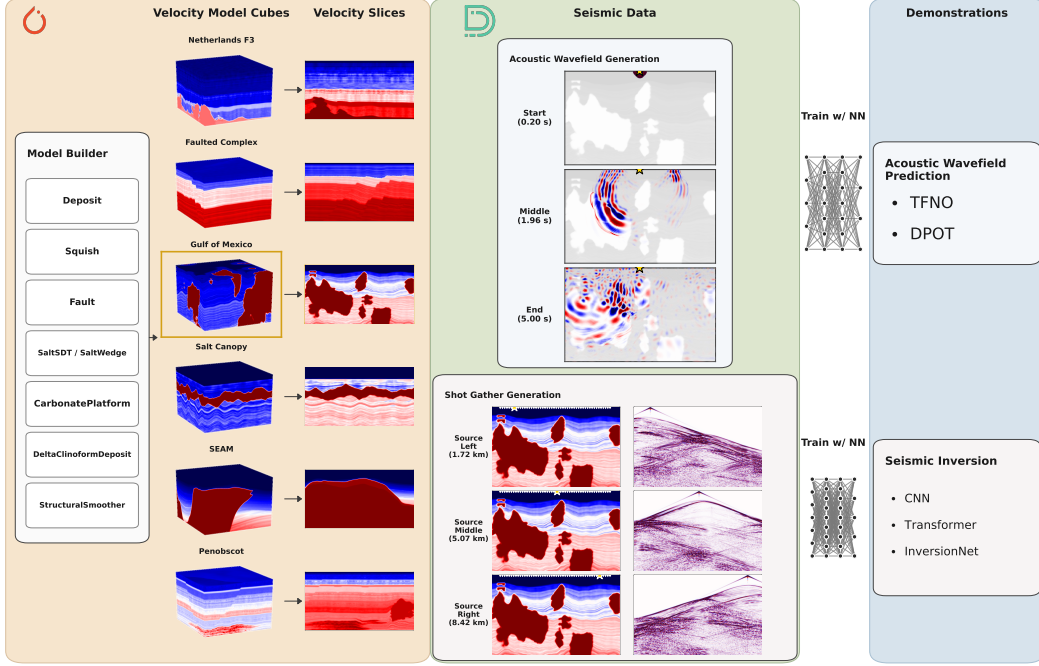


Figure 1: SubsurfaceGen is a GPU-accelerated velocity model builder (using PyTorch) and seismic data generator (using Devito), which can be used to produce training data for ML-based FWI. We use SubsurfaceGen to create a dataset of 42 realistic, field-scale 3D velocity models along with (velocity slice, wavefield) and (velocity model, shot gather) pairs. We use these pairs to train neural operators for wavefield prediction and encoder–decoders for end-to-end inversion from shot gathers.

optimal checkpointing [Symes, 2007]; for end-to-end inversion, geological diversity supports cross-geology generalization studies, opening a new possibility for evaluating architectures.

The rest of the paper proceeds as follows: Section 2 introduces the acoustic wave equation, Sections 3 and 4 describe SubsurfaceGen’s velocity model and seismic data generation components, Sections 5 and 6 present our experiments for ML-based FWI, and Section A covers related work.

## 2 The Acoustic Wave Equation

The acoustic wave equation maps a velocity model  $v_p(\mathbf{x})$  to a wavefield  $p(\mathbf{x}, t)$  that would be recorded in a real-world seismic survey. This mapping is central to FWI and the ML methods in Section 1: FWI inverts it, neural operators approximate it, and encoder–decoders for end-to-end inversion are trained against data produced by it. SubsurfaceGen solves the 2D acoustic, constant-density, isotropic form of the wave equation with a source term:

$$\frac{1}{v_p(\mathbf{x})^2} \frac{\partial^2 p(\mathbf{x}, t)}{\partial t^2} - \nabla^2 p(\mathbf{x}, t) = s(\mathbf{x}, t). \quad (1)$$

Here  $\mathbf{x} = (x, z)$  is the spatial coordinate (lateral  $x$ , depth  $z$ ),  $t$  is time,  $p(\mathbf{x}, t)$  is the wavefield,  $v_p(\mathbf{x})$  is the velocity model,  $\nabla^2 = \partial_x^2 + \partial_z^2$  is the Laplacian, and  $s(\mathbf{x}, t)$  is the source term. SubsurfaceGen models the source  $s(\mathbf{x}, t)$  as a Ricker wavelet [Ricker, 1953], which is standard in seismic processing [Wang, 2015]. Initial and boundary conditions are deferred to Section E.

Solving (1) produces the wavefield  $p(\mathbf{x}, t)$  across space and time. However, the wavefield is not observed at all spatial locations in a seismic survey. Seismic surveys place a sparse line of sensors at the surface, called *receivers*, that record the time history of the wavefield. SubsurfaceGen reproduces this with a sampling operator  $\mathcal{R}$  that observes the wavefield  $p$  at the receiver locations: the result is a shot gather  $\mathcal{R}p$ , a 2D tensor with axes for time and receiver index. The remaining challenge is generating diverse, realistic velocity models, which we address in Section 3.

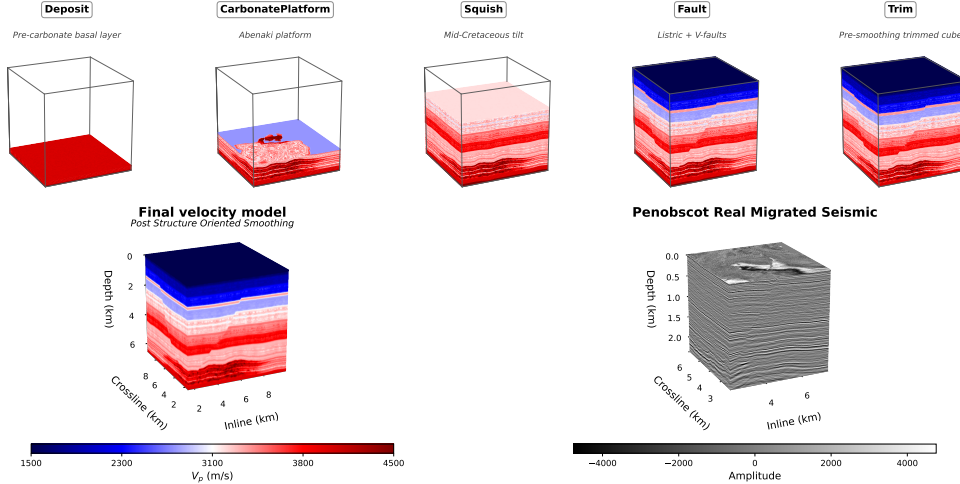


Figure 2: Top: Step-by-step construction of a Penobscot velocity model using SubsurfaceGen modules (we omit some steps for simplicity). Bottom: The velocity model juxtaposed against the Penobscot migrated cube. The velocity model captures key geological features of the migrated cube.

### 3 SubsurfaceGen: Procedural Velocity Model Generation

SubsurfaceGen provides functionality for generating realistic, field-scale 3D velocity models using a catalog of modules that emulate geological features observed in real-world seismic data. These modules include interbeds, faults, salt bodies, clinoforms, and carbonate platforms, which are essential for characterizing sedimentary settings that arise in carbon sequestration and hydrocarbon exploration. We have written SubsurfaceGen’s model building functionality in PyTorch, which enables GPU-accelerated velocity model generation, making it easier for practitioners to generate large datasets of velocity models. We also describe our process for generating velocity models that are contained in the field-scale dataset on Hugging Face. Additional details are available in Sections B to D.

#### 3.1 Velocity Model Builder

**The module catalog.** SubsurfaceGen introduces eight modules for building velocity models. Three of them (Deposit, Squish, Fault) improve on the synthetic-model package from Clapp [2018, 2022, 2024]. The remaining five modules (SaltSDT, SaltWedge, CarbonatePlatform, DeltaClinoformDeposit, StructuralSmoother) are original to SubsurfaceGen. At a high level: Deposit adds stratified layers, Squish warps layers into folds, Fault cuts and shifts layers, SaltSDT emplaces salt bodies and SaltWedge deforms layers around them, CarbonatePlatform builds reef structures, DeltaClinoformDeposit places deltaic formations, and StructuralSmoother applies geology-aware smoothing. Table 5 provides a full description of each module.

**Building velocity models.** Velocity models are built by *applying* the modules in sequence, starting from a flat, homogeneous volume (called the *basement*) and adding modules going up to the surface. Each module takes the current velocity model as input and modifies it according to its specific geological feature. The order of module application follows geological time, with older features laid down before younger ones. After all modules have been applied, the user can apply structure-oriented smoothing (SOS) [Hale, 2009] via StructuralSmoother to remove numerical artifacts from the build process while preserving important geological features like faults and bed contacts. The model building process is highly customizable, allowing users to specify parameters for each module to generate a variety of velocity models that capture the diversity of geological settings observed in real subsurface scenarios. Fig. 2 illustrates this process for a Penobscot velocity model.

**GPU generation makes SubsurfaceGen extensible.** Table 2 reports per-setting build times on GPU vs. CPU: GPU yields a  $7.2\times$ – $26.8\times$  speedup, bringing build times down from 1–2 hours on

CPU to 5–10 minutes on GPU. This makes SubsurfaceGen particularly useful for practitioners who want to adapt it to a new geological setting or study scaling behavior.

Table 2: Total build time per geological setting. GPU: one 80 GB NVIDIA A100. CPU: 16 cores of an AMD EPYC 7763 with 256 GB of RAM. A full breakdown of the timings is in Section D.

Setting	GPU build (min)	CPU build (min)	Speedup
Penobscot	5.57	92.67	16.6×
F3	11.49	82.29	7.2×
Fault	5.84	156.57	26.8×
Gulf of Mexico	6.70	100.21	15.0×

### 3.2 Generation of Field-Scale Velocity Models for Hugging Face Dataset

**Building the dataset with SubsurfaceGen.** We use SubsurfaceGen to generate the velocity models in our Hugging Face dataset, building each model by applying modules from basement to surface. The dataset contains 42 field-scale velocity models in total, each  $6.19 \text{ km} \times 10 \text{ km} \times 10 \text{ km}$  at 10 m resolution, organized into six geological settings. Four of the settings (Penobscot, F3, Gulf of Mexico, Fault) are SubsurfaceGen builds. The remaining two are not: SEAM is an existing model [Fehler and Keliher, 2011] and Salt Canopy was generated using a legacy model building code with inspiration from Farris et al. [2023]. A full inventory is given in Table 6 of Section C.

**Diversity between and within geological settings.** Our velocity models are designed to mimic publicly-available *migrated cubes*—estimates of subsurface structure reconstructed from seismic reflection data recorded at the surface [Lo and Inderwiesen, 1994], similar to the way in which medical CT scans estimate internal anatomy from X-ray attenuation measurements taken outside the body. The velocity models in our dataset capture diversity across two levels: *between geological settings* and *within each setting*. We provide six settings (Penobscot, F3, Gulf of Mexico, Fault, Salt Canopy, SEAM) so that downstream models see a wide variety of geological features. Within each setting, we provide multiple realizations drawn from the same regional distribution (we describe our methodology in the next paragraph). Publicly-available migrated cubes are scarce, so within-setting diversity allows us to leverage the few cubes that do exist while still providing enough velocity models for training.

**Matching to migrated cubes and sampling variants.** We match a velocity model for each setting to the corresponding migrated cube, then sample variants around the matched parameters. The build process is the deterministic mapping  $\mathcal{M}(\theta) = V$ , where  $\mathcal{M}$  denotes the velocity model builder,  $\theta$  denotes the parameter vector configuring SubsurfaceGen modules, and  $V$  denotes the resulting velocity model. Matching is manual: given a public migrated cube  $C_{\text{GT}}$ , we pick a parameter vector  $\theta$ , generate  $\mathcal{M}(\theta)$ , compare to  $C_{\text{GT}}$  by visual inspection, and iterate until  $\mathcal{M}(\theta_{\text{cal}})$  resembles  $C_{\text{GT}}$ . We then define a sampling distribution  $\mathcal{D}$  centered at  $\theta_{\text{cal}}$ , draw

$$\theta_1, \dots, \theta_k \stackrel{\text{iid}}{\sim} \mathcal{D},$$

and produce the setting’s models as  $\mathcal{M}(\theta_{\text{cal}}), \mathcal{M}(\theta_1), \dots, \mathcal{M}(\theta_k)$ . Fig. 2 shows the public migrated cube  $C_{\text{GT}}$  alongside our matched synthetic  $\mathcal{M}(\theta_{\text{cal}})$  for the Penobscot setting; per-setting geological details and build scripts are in Section C.

## 4 SubsurfaceGen: Seismic Data Generation

We describe the seismic data generation functionality of SubsurfaceGen and explain how we use it to build the seismic data in our Hugging Face dataset. For each 3D velocity model from Section 3, we extract 2D slices and solve the acoustic wave equation (1) on each slice to obtain the corresponding wavefields and shot gathers. We repeat this for five different source bandwidths (Table 14), motivated by multiscale FWI [Bunks et al., 1995, Fichtner, 2011], where practitioners progressively increase the source bandwidth to mitigate cycle skipping. For additional details on the seismic data generation process, see Section E.

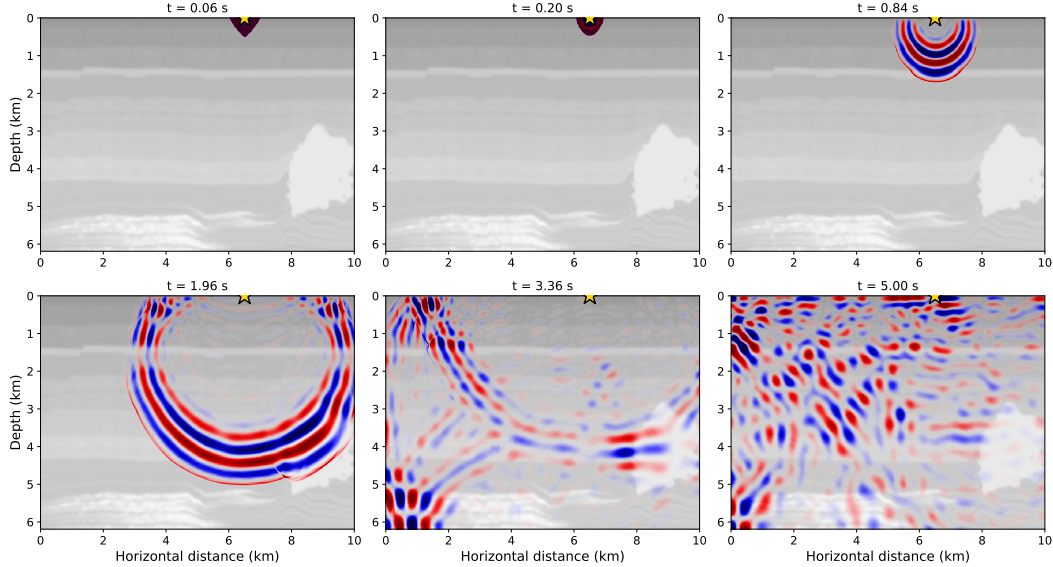


Figure 3: Wavefield evolution on a Penobscot crossline slice with a Ricker wavelet source near the surface. Waves radiate outward from the source until they enter a salt body (1.96 s), with chaotic multipath behavior dominating at late times (5.0 s).

#### 4.1 Seismic Data Generator

SubsurfaceGen extracts 2D slices from a 3D velocity model along a horizontal axis (inline or crossline). SubsurfaceGen uses Devito [Louboutin et al., 2019] to solve (1) for each slice at a user-specified spatial discretization and time discretization, simulation time, source bandwidth, and source position. The source  $s(\mathbf{x}, t)$  is a Ricker wavelet, as motivated in Section 2. The user can save the wavefield  $p(\mathbf{x}, t)$  and/or the shot gather  $\mathcal{R}p$ .

#### 4.2 Generation of Seismic Data for Hugging Face Dataset

**Slice configuration.** For all 42 velocity models from Section 3.2, we randomly draw 2D slices along the inline and crossline axes, with half of the slices coming from each orientation. Each slice is of size  $619 \times 1000$  at 10 m grid spacing; per-setting slice counts are listed in Table 3.

**Wavefields and shot gathers.** Our dataset targets marine acquisitions: for each slice, we solve the acoustic wave equation (1) with Devito on a 10 m grid, setting the source  $s(\mathbf{x}, t)$  to be a Ricker wavelet near the surface to emulate an air gun towed behind a vessel. We generate wavefields by using a single source at a random horizontal position, simulating for 5 s, and saving the wavefield  $p(\mathbf{x}, t)$  as a tensor of shape  $358 \times 619 \times 1000$ ; Fig. 3 shows a wavefield generated from a Penobscot slice. We generate shot gathers by using 64 equally-spaced sources and 1000 equally-spaced receivers, simulating for 8 s (long enough for the deepest reflections to return to the surface), and aggregating the individual shot gathers  $\mathcal{R}p$  as a *shot-gather cube* of shape  $64 \times 572 \times 1000$ . Representative gathers from three training settings appear in Fig. 11.

**Dataset splits.** We construct two test sets (Table 3). The in-distribution test set draws slices from the same five settings as training, but at non-overlapping positions within each velocity model. The out-of-distribution test set is Penobscot, which we hold out from training entirely to evaluate generalization to unseen geology.

Table 3: Dataset split. Each slice is paired with a wavefield and a shot-gather cube at every frequency band, yielding  $(4,096 + 100 + 80) \cdot 5 = 21,380$  wavefields and 21,380 shot-gather cubes.

Split	# Slices	Model Types
Train	4,096	F3, GoM, Fault, Salt Canopy, SEAM
Test in-dist	100	Same settings, non-overlapping slices
Test out-of-dist	80	Penobscot only

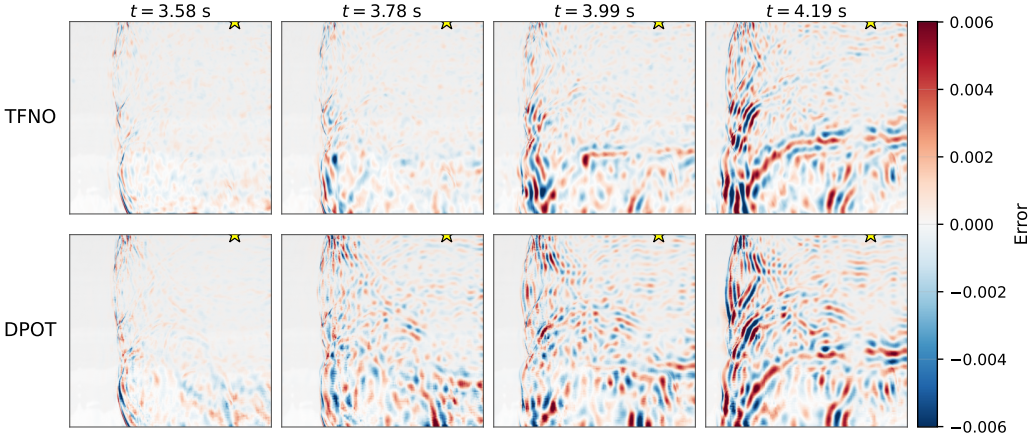


Figure 4: Wavefield prediction error for TFNO (top) and DPOT (bottom) on the F3 example slice over a single chunk at late propagation. Errors concentrate where the wavefield is most chaotic, illustrating the late-time scattering both networks struggle to reproduce.

## 5 Wavefield Prediction with Neural Operators

We train neural operators to predict wavefields—an alternative to the expensive PDE solves that dominate FWI’s compute cost. At field scale, predicting the full  $T = 348$  frame trajectory on the  $619 \times 1000$  grid in one forward pass exceeds GPU memory, forcing a *chunked autoregressive rollout*: each chunk takes the last  $t_{\text{in}} = 10$  frames, the velocity model, and a source mask, predicts the next  $t_{\text{out}} = 50$  frames, and feeds its output into the next chunk. This regime does not arise on smaller datasets like OpenFWI, where a single forward pass fits in memory. We compare two architecturally distinct neural operators, TFNO [Kossaifi et al., 2024] and DPOT [Hao et al., 2024], trained for 10 epochs on a single seed (full hyperparameters and architecture details in Section F). One F3 test slice serves as a running example throughout this section.

Fig. 4 shows TFNO and DPOT prediction error on a single chunk of the F3 example slice at late propagation time, where reflections from the salt body produce chaotic multipath interference. Both architectures track the dominant wavefronts well, with errors concentrated in deep regions. Per-geology and per-wavenumber breakdowns of TFNO and DPOT performance are in Section F.7.

Fig. 6 shows the cost of chunked autoregressive rollout over the entire  $T = 348$  frame trajectory: the L2 relative error (L2RE) compounds by roughly an order of magnitude from one chunk to the end—though the dominant reflections remain visible in both models’ predictions out to several seconds. The field-scale dataset enables this regime in the first place: at the shorter propagation times of smaller datasets like OpenFWI (1 s vs. our 5 s), no chunking would be required, so the long-horizon failure modes we observe here would not arise.

FWI manages a similar storage-vs-compute trade-off via optimal checkpointing [Symes, 2007]: anchor wavefield states are stored at sparse times and the wavefield is recomputed between them by finite-difference solves. We adapt optimal checkpointing to neural operators by filling a  $\tau = 20$  frame interior gap between two stored anchor windows of  $T_L = T_R = 20$  frames on each side, with the prediction pinned to the anchor frames at the gap boundaries (full architecture in Section F.2); we call this variant *TFNO-interp*. Anchoring at the gap boundaries uniformly reduces drift: Fig. 5 shows

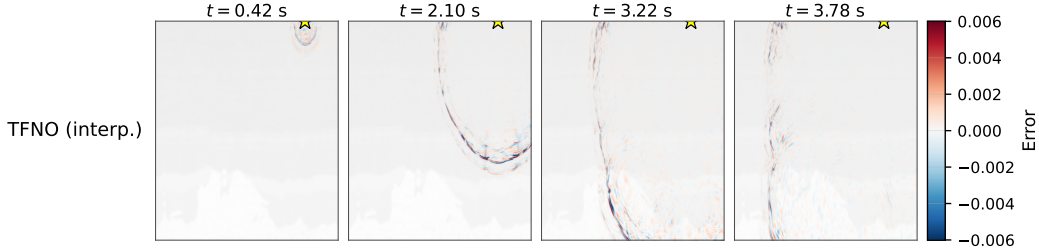


Figure 5: TFNO-interp prediction error on the same F3 example slice, sampled at four interior gap centers over the full trajectory. TFNO-interp’s error is visibly lower than TFNO’s and DPOT’s, and the gap-centered sampling shows that the improvement is not just near the anchor frames.

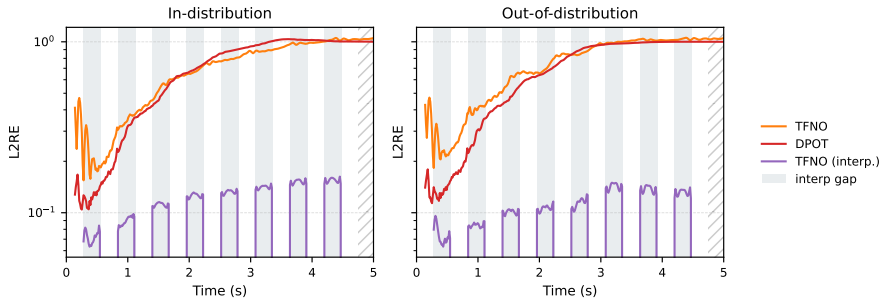


Figure 6: L2RE versus propagation time for TFNO, DPOT, and TFNO-interp on the in-distribution and out-of-distribution test sets. The forward operators’ (TFNO, DPOT) error compounds over time; TFNO-interp’s prediction windows (shaded light gray) stay roughly an order of magnitude lower.

it qualitatively on the F3 example, and Fig. 6 confirms TFNO-interp’s L2RE in the gap intervals is roughly  $6\times$  lower than either forward operator’s at every time step. These experiments show the value of the field-scale dataset: the drift on chunked rollout and the analogy to optimal checkpointing both surface at field-scale, motivating TFNO-interp.

## 6 End-to-End Inversion with Encoder–Decoders

We train networks that map a 3D shot-gather cube directly to the corresponding 2D velocity model  $v_p(\mathbf{x})$ —an alternative to classical FWI that could avoid cycle skipping and the cost of repeated PDE solves. To our knowledge, our dataset is the first to enable cross-geology generalization studies on this task at field-scale: Marmousi and SEAM each contain only one geological setting, and OpenFWI evaluates cross-geology generalization, but only on  $0.7\text{ km} \times 0.7\text{ km}$  models.

We compare three encoder–decoder architectures: **InversionNet** [Wu and Lin, 2020] treats the shot-gather cube as a 2D image with 64 channels; **Transformer** [Liu et al., 2021, Hatamizadeh et al., 2022] and **CNN** [Isensee et al., 2024] treat it as a 3D volume. The Transformer and CNN share an identical decoder architecture, so any gap between them is attributable to the encoder. We train each architecture for 100 epochs across three seeds and report root mean square error (RMSE) and structural similarity (SSIM) [Wang et al., 2004] on the three splits (Table 3), where Penobscot is held out as the out-of-distribution (OOD) test split. Full details are available in Section G.

Table 4 reports RMSE and SSIM across the three splits and Fig. 7 shows prediction errors on the in-distribution test split. The CNN captures large-scale geological features (salt bodies, faults) better than the other two architectures, but all three architectures struggle to resolve fine-scale features. Moreover, the CNN uniformly outperforms InversionNet, showing the value of a 3D representation in the encoder. The Penobscot hold-out lets us understand how each architecture generalizes to a new geological setting: the Transformer’s SSIM is stable while the CNN’s and InversionNet’s drop by 0.04–0.07, revealing a relationship between architecture and OOD performance.

Table 4: End-to-end inversion accuracy across architectures and splits (averaged over 3 seeds).

Architecture	RMSE (m/s) ↓			SSIM ↑		
	Train	Test (in-dist.)	Test (out-of-dist.)	Train	Test (in-dist.)	Test (out-of-dist.)
InversionNet	72.18	260.32	603.09	0.909	0.893	0.848
Transformer	141.45	239.87	526.44	0.881	0.892	0.883
CNN	55.72	135.75	458.58	0.923	0.923	0.851

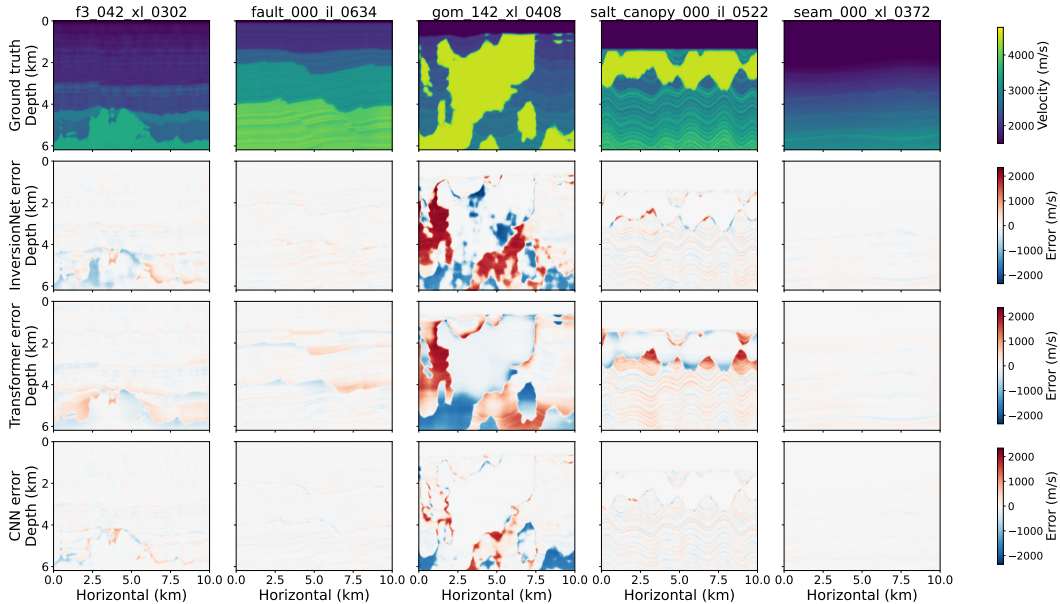


Figure 7: Inverted velocity models on the in-distribution test split (one slice per setting: F3, Fault, Gulf of Mexico, Salt Canopy, SEAM). Top row: ground-truth velocity. Subsequent rows: prediction error for InversionNet, Transformer, and CNN.

## 7 Conclusion

We introduce SubsurfaceGen, a GPU-accelerated procedural velocity model builder and seismic data generator for ML-based FWI. We use SubsurfaceGen to generate an example field-scale dataset, available on Hugging Face. Our experiments reveal how SubsurfaceGen can impact ML-based FWI: for wavefield prediction, the field-scale grid forces predictions to be chunked, which motivates checkpointing strategies; for end-to-end inversion, geological diversity supports cross-geology generalization studies, opening a new possibility for evaluating architectures. Natural extensions include wavefield and shot gather generation over 3D domains and modeling with the elastic wave equation.

## Impact Statement

SubsurfaceGen and the field-scale dataset democratize ML for seismic imaging by lowering the barrier to entry for researchers who lack proprietary seismic data. SubsurfaceGen and the field-scale dataset can be applied for verifying the integrity of carbon sequestration sites (climate-positive) and for hydrocarbon exploration, which is a significant driver of greenhouse gas emissions (climate-negative); the net environmental impact depends on who builds upon this work and how they use it. The field-scale dataset is intended to support ML method development and could serve as a foundation for future benchmarks, but we caution against deploying models trained on it in real-world settings without further validation and testing.

## Acknowledgments and Disclosure of Funding

We would like to thank Bob Clapp for creating the first version of the velocity model builder and Rustam Akhmadiev for suggesting the checkpointing idea. We would also like to thank Elliana Abrahams, Guillaume Barnier, Ettore Biondi, Brian Chivers, Thomas Cullison, Stuart Farris, Zachary Frangella, Wenzhi Gao, Joshua Rines, Drew Stump, Yinjun Wang, and Anders Wikum for valuable feedback that helped shape this submission. JS acknowledges support from the Stanford Geophysics Ph.D. program, including the secondary research project completed under the advising of CYL as part of the Ph.D. breadth requirement, and graduate research support under the advising of Biondo Biondi. PR and MU gratefully acknowledge support from the Office of Naval Research under award N000142412306, Air Force Office of Scientific Research under award FA9550-26-1-0012, the Alfred P. Sloan Foundation, the Stanford Institute for Human-Centered Artificial Intelligence, and from IBM Research as a founding member of Stanford Institute for Human-centered Artificial Intelligence. CYL gratefully acknowledges support from the Alfred P. Sloan Foundation via grant FG-2024-21649. We acknowledge Stanford University and the Center for Computation at the Stanford Doerr School of Sustainability for computational resources and support, including access to the Sherlock computing cluster and the serc partition. We also acknowledge computational resources provided through allocation EES260056 from the Advanced Cyberinfrastructure Coordination Ecosystem: Services & Support (ACCESS) program, supported by the U.S. National Science Foundation.

## References

- Mauricio Araya-Polo, Joseph Jennings, Amir Adler, and Taylor Dahlke. Deep-learning tomography. *The Leading Edge*, 37(1):58–66, 2018.
- M. E. Badley, J. D. Price, C. Rambech Dahl, and T. Agdestein. The structural evolution of the northern Viking Graben and its bearing upon extensional modes of basin formation. *Journal of the Geological Society*, 145(3):455–472, 1988.
- Guillaume Barnier, Ettore Biondi, Robert G. Clapp, and Biondo Biondi. Full-waveform inversion by model extension: Practical applications. *Geophysics*, 88(5):R609–R643, 2023.
- Lais Baroni, Reinaldo Mozart Silva, Rodrigo S. Ferreira, Daniel Civitaresi, Daniela Szwarcman, and Emilio Vital Brazil. Penobscot dataset: Fostering machine learning development for seismic interpretation. *arXiv preprint arXiv:1903.12060*, 2019.
- Biondo Biondi and Ali Almomin. Simultaneous inversion of full data bandwidth by tomographic full-waveform inversion. *Geophysics*, 79(3):WA129–WA140, 2014.
- D. E. Brown. *Regional Geology of the Scotian Basin*. Canada-Nova Scotia Offshore Petroleum Board, 2008.
- Carey Bunks, Fatimetou M. Saleck, S. Zaleski, and G. Chavent. Multiscale seismic waveform inversion. *Geophysics*, 60(5):1457–1473, 1995.
- Charles Cerjan, Dan Kosloff, Ronnie Kosloff, and Moshe Reshef. A nonreflecting boundary condition for discrete acoustic and elastic wave equations. *Geophysics*, 50(4):705–708, 1985.
- Robert G. Clapp. Synthetic model building for training neural networks in a Jupyter notebook. Technical Report SEP-172, Stanford Exploration Project, 2018.
- Robert G. Clapp. Generating synthetic models for machine learning. Technical Report SEP-187, Stanford Exploration Project, 2022.
- Robert G. Clapp. synthetic-model: A library for creating synthetic geologic velocity models, 2024. URL <https://github.com/SEP-software/synthetic-model>.
- Oluwaseun E. Coker, He Wang, Amirul Khan, and Peter K. Jimack. Scheduled temporal loss weighting for neural operators. In *NeurIPS Workshop on Machine Learning and the Physical Sciences*, 2025.
- R. Courant, K. Friedrichs, and H. Lewy. Über die partiellen differenzgleichungen der mathematischen physik. *Mathematische Annalen*, 100(1):32–74, 1928.

- P. A. Cowie and C. H. Scholz. Displacement-length scaling relationship for faults: Data synthesis and discussion. *Journal of Structural Geology*, 14(10):1149–1156, 1992.
- I. Davison, I. Alsop, P. Birch, C. Elders, N. Evans, H. Nicholson, P. Rorison, D. Wade, J. Woodward, and M. Young. Geometry and late-stage structural evolution of central Graben salt diapirs, North Sea. *Marine and Petroleum Geology*, 17(4):499–522, 2000.
- Miguel de la Varga, Alexander Schaaf, and Florian Wellmann. GemPy 1.0: open-source stochastic geological modeling and inversion. *Geoscientific Model Development*, 12(1):1–32, 2019.
- Chengyuan Deng, Shihang Feng, Hanchen Wang, Xitong Zhang, Peng Jin, Yinan Feng, Qili Zeng, Yinpeng Chen, and Youzuo Lin. OpenFWI: Large-scale multi-structural benchmark datasets for full waveform inversion. In *Advances in Neural Information Processing Systems, Datasets and Benchmarks Track*, 2022.
- F. A. Diegel, J. F. Karlo, D. C. Schuster, R. C. Shoup, and P. R. Tauvers. Cenozoic structural evolution and tectono-stratigraphic framework of the northern Gulf Coast continental margin. In M. P. A. Jackson, D. G. Roberts, and S. Snelson, editors, *Salt Tectonics: A Global Perspective*, volume 65 of *AAPG Memoir*, pages 109–151. American Association of Petroleum Geologists, 1995.
- L. S. Eliuk. The Abenaki Formation, Nova Scotia Shelf, Canada — a depositional and diagenetic model for a mesozoic carbonate platform. *Bulletin of Canadian Petroleum Geology*, 26(4):424–514, 1978.
- Stuart Farris. *Seismic Velocity Model Building with Deep Convolutional Neural Networks*. Ph.d. thesis, Stanford University, 2023. Stanford Exploration Project report SEP-190.
- Stuart Farris, Robert Clapp, and Mauricio Araya-Polo. Learning-based seismic velocity inversion with synthetic and field data. *Sensors*, 23(19), 2023.
- Michael Fehler and P. Joseph Keliher. *SEAM Phase I: Challenges of Subsalt Imaging in Tertiary Basins, with Emphasis on Deepwater Gulf of Mexico*. Society of Exploration Geophysicists, 2011.
- Shihang Feng, Hanchen Wang, Chengyuan Deng, Yinan Feng, Yanhua Liu, Min Zhu, Peng Jin, Yinpeng Chen, and Youzuo Lin.  $\mathbb{E}^{\text{FWI}}$ : Multiparameter benchmark datasets for elastic full waveform inversion of geophysical properties. In *Advances in Neural Information Processing Systems, Datasets and Benchmarks Track*, 2023.
- Andreas Fichtner. *Full Seismic Waveform Modelling and Inversion*. Advances in Geophysical and Environmental Mechanics and Mathematics. Springer, 2011.
- Bengt Fornberg. Generation of finite difference formulas on arbitrarily spaced grids. *Mathematics of Computation*, 51(184):699–706, 1988.
- R. L. Gawthorpe and M. R. Leeder. Tectono-sedimentary evolution of active extensional basins. *Basin Research*, 12(3–4):195–218, 2000.
- Katherine A. Giles and Mark G. Rowan. Concepts in halokinetic-sequence deformation and stratigraphy. *Geological Society, London, Special Publications*, 363(1):7–31, 2012.
- Lachlan Grose, Laurent Ailleres, Gautier Laurent, and Mark Jessell. LoopStructural 1.0: time-aware geological modelling. *Geoscientific Model Development*, 14(6):3915–3937, 2021.
- Dave Hale. Structure-oriented smoothing and semblance. *CWP Report*, 635, 2009.
- Zhongkai Hao, Chang Su, Songming Liu, Julius Berner, Chengyang Ying, Hang Su, Anima Anandkumar, Jian Song, and Jun Zhu. DPOT: Auto-regressive denoising operator transformer for large-scale PDE pre-training. In *Forty-first International Conference on Machine Learning*, 2024.
- Ali Hatamizadeh, Vishwesh Nath, Yucheng Tang, Dong Yang, Holger R. Roth, and Daguang Xu. Swin UNETR: Swin transformers for semantic segmentation of brain tumors in MRI images. In *Brainlesion: Glioma, Multiple Sclerosis, Stroke and Traumatic Brain Injuries*, pages 272–284, 2022.

- William Helland-Hansen and Gary J. Hampson. Trajectory analysis: Concepts and applications. *Basin Research*, 21(5):454–483, 2009.
- Xinquan Huang and Tariq Alkhalifah. Learned frequency-domain scattered wavefield solutions using neural operators. *Geophysical Journal International*, 241(3):1467–1485, 2025.
- Michael R. Hudec and Martin P. A. Jackson. Advance of allochthonous salt sheets in passive margins and orogens. *AAPG Bulletin*, 90(10):1535–1564, 2006.
- Michael R. Hudec and Martin P. A. Jackson. Terra infirma: Understanding salt tectonics. *Earth-Science Reviews*, 82(1–2):1–28, 2007.
- Michael R. Hudec, Ian O. Norton, Martin P. A. Jackson, and Frank J. Peel. Jurassic evolution of the Gulf of Mexico salt basin. *AAPG Bulletin*, 97(10):1683–1710, 2013.
- Fabian Isensee, Tassilo Wald, Constantin Ulrich, Michael Baumgartner, Saikat Roy, Klaus Maier-Hein, and Paul F. Jaeger. nnU-Net revisited: A call for rigorous validation in 3D medical image segmentation, 2024. arXiv:2404.09556.
- Martin P. A. Jackson and Michael R. Hudec. *Salt Tectonics: Principles and Practice*. Cambridge University Press, 2017.
- Peng Jin, Yanan Feng, Shihang Feng, Hanchen Wang, Yinpeng Chen, Benjamin Consolvo, Zicheng Liu, and Youzuo Lin. An empirical study of large-scale data-driven full waveform inversion. *Scientific Reports*, 14, 2024.
- Ian F. Jones and Ian Davison. Seismic imaging in and around salt bodies. *Interpretation*, 2(4):SL1–SL20, 2014.
- A. G. Kidston, D. E. Brown, B. M. Smith, and B. Altheim. *Hydrocarbon Potential of the Deep-Water Scotian Slope*. Canada-Nova Scotia Offshore Petroleum Board, 2002.
- Jean Kossaifi, Nikola Kovachki, Kamyar Azizzadenesheli, and Anima Anandkumar. Multi-grid tensorized Fourier neural operator for high-resolution PDEs. *Transactions on Machine Learning Research*, 2024.
- G. Kuhlmann, C. G. Langereis, D. Munsterman, R.-J. van Leeuwen, R. Verreussel, J. E. Meulenkaamp, and Th. E. Wong. Integrated chronostratigraphy of the Pliocene-Pleistocene interval and its relation to the regional stratigraphical stages in the southern North Sea region. *Netherlands Journal of Geosciences*, 85(1):19–35, 2006.
- Patrick Lailly. The seismic inverse problem as a sequence of before stack migrations. In *Conference on Inverse Scattering: Theory and Application*, 1983.
- Shiqian Li, Zhi Li, Zhancun Mu, Shiji Xin, Zhixiang Dai, Kuangdai Leng, Ruihua Zhang, Xiaodong Song, and Yixin Zhu. GlobalTomo: A global dataset for physics-ML seismic wavefield modeling and FWI. In *Advances in Neural Information Processing Systems, Datasets and Benchmarks Track*, 2025.
- Zongyi Li, Nikola Kovachki, Kamyar Azizzadenesheli, Burigede Liu, Kaushik Bhattacharya, Andrew Stuart, and Anima Anandkumar. Fourier neural operator for parametric partial differential equations. In *International Conference on Learning Representations*, 2021.
- Yang Liu and Mrinal K. Sen. A new time–space domain high-order finite-difference method for the acoustic wave equation. *Journal of Computational Physics*, 228(23):8779–8806, 2009.
- Ze Liu, Yutong Lin, Yue Cao, Han Hu, Yixuan Wei, Zheng Zhang, Stephen Lin, and Baining Guo. Swin transformer: Hierarchical vision transformer using shifted windows. In *Proceedings of the IEEE/CVF International Conference on Computer Vision*, 2021.
- Tien-When Lo and Philip L. Inderwiesen. *Fundamentals of Seismic Tomography*. Number 6 in Geophysical Monograph Series. Society of Exploration Geophysicists, 1994.

- M. Louboutin, M. Lange, F. Luporini, N. Kukreja, P. A. Witte, F. J. Herrmann, P. Velesko, and G. J. Gorman. Devito (v3.1.0): an embedded domain-specific language for finite differences and geophysical exploration. *Geoscientific Model Development*, 12(3):1165–1187, 2019.
- Gary S. Martin, Robert Wiley, and Kurt J. Marfurt. Marmousi2: An elastic upgrade for marmousi. *The Leading Edge*, 25(2):156–166, 2006.
- Tom P. Merrifield, Donald P. Griffith, S. Ahmad Zamanian, Stephane Gesbert, Satyakee Sen, Jorge De La Torre Guzman, R. David Potter, and Henning Kuehl. Synthetic seismic data for training deep learning networks. *Interpretation*, 10(3):SE31–SE39, 2022.
- R. M. Mitchum, Jr., P. R. Vail, and J. B. Sangree. Seismic stratigraphy and global changes of sea level, part 6: Stratigraphic interpretation of seismic reflection patterns in depositional sequences. In C. E. Payton, editor, *Seismic Stratigraphy — Applications to Hydrocarbon Exploration*, volume 26 of *AAPG Memoir*, pages 117–133. American Association of Petroleum Geologists, 1977.
- C. K. Morley. Patterns of displacement along large normal faults: Implications for basin evolution and fault propagation, based on examples from East Africa. *AAPG Bulletin*, 83(4):613–634, 1999.
- Lukas Mosser, Olivier Dubrulle, and Martin J. Blunt. Stochastic seismic waveform inversion using generative adversarial networks as a geological prior. *Mathematical Geosciences*, 52(1):53–79, 2020.
- A. Nicol, J. Watterson, J. J. Walsh, and C. Childs. The shapes, major axis orientations and displacement patterns of fault surfaces. *Journal of Structural Geology*, 18(2–3):235–248, 1996.
- Irina Overeem, Gert Jan Weltje, Claire Bishop-Kay, and Salomon B. Kroonenberg. The late cenozoic Eridanos delta system in the southern North Sea basin: A climate signal in sediment supply? *Basin Research*, 13(3):293–312, 2001.
- D. C. P. Peacock and D. J. Sanderson. Geometry and development of relay ramps in normal fault systems. *AAPG Bulletin*, 78(2):147–165, 1994.
- F. J. Peel, C. J. Travis, and J. R. Hossack. Genetic structural provinces and salt tectonics of the Cenozoic offshore U.S. Gulf of Mexico: A preliminary analysis. In M. P. A. Jackson, D. G. Roberts, and S. Snelson, editors, *Salt Tectonics: A Global Perspective*, volume 65 of *AAPG Memoir*, pages 153–175. American Association of Petroleum Geologists, 1995.
- Robin S. Pilcher, Bill Kilsdonk, and James Trude. Primary basins and their boundaries in the deep-water northern Gulf of Mexico: Origin, trap types, and petroleum system implications. *AAPG Bulletin*, 95(2):219–240, 2011.
- Norman Ricker. The form and laws of propagation of seismic wavelets. *Geophysics*, 18(1):10–40, 1953.
- Paul Sava and Biondo Biondi. Wave-equation migration velocity analysis. I. Theory. *Geophysical Prospecting*, 52(6):593–606, 2004a.
- Paul Sava and Biondo Biondi. Wave-equation migration velocity analysis. II. Subsalt imaging examples. *Geophysical Prospecting*, 52(6):607–623, 2004b.
- Alan Schiemenz and Heiner Igel. Accelerated 3-D full-waveform inversion using simultaneously encoded sources in the time domain: application to Valhall ocean-bottom cable data. *Geophysical Journal International*, 195(3):1970–1988, 2013.
- Reinaldo Mozart Silva, Lais Baroni, Rodrigo S. Ferreira, Daniel Civitarese, Daniela Szwarcman, and Emilio Vital Brazil. Netherlands dataset: A new public dataset for machine learning in seismic interpretation. *arXiv preprint arXiv:1904.00770*.
- Society of Exploration Geophysicists. SEAM Open Data. <https://seg.org/SEAM/open-data/>, 2024.
- Joseph Stitt, Robert Clapp, and Biondo Biondi. Deep Dix: Enhancing interval velocity model estimation through adversarial regularization. In *Third International Meeting for Applied Geoscience & Energy (SEG IMAGE 2023)*, *Technical Program Expanded Abstracts*, pages 108–112, 2023.

- Joseph Stitt, Robert Clapp, and Biondo Biondi. Latent diffusion regularization on FWI. Technical Report SEP-196, Stanford Exploration Project, 2025.
- William W. Symes. Reverse time migration with optimal checkpointing. *Geophysics*, 72(5):SM213–SM221, 2007.
- William W. Symes. Migration velocity analysis and waveform inversion. *Geophysical Prospecting*, 56(6):765–790, 2008.
- Albert Tarantola. Inversion of seismic reflection data in the acoustic approximation. *Geophysics*, 49(8):1259–1266, 1984.
- J. R. Underhill and M. A. Partington. Jurassic thermal doming and deflation in the North Sea: Implications of the sequence stratigraphic evidence. In J. R. Parker, editor, *Petroleum Geology of Northwest Europe: Proceedings of the 4th Conference*, volume 4 of *Geological Society, London, Petroleum Geology Conference Series*, pages 337–345. Geological Society of London, 1993.
- Roelof Versteeg. The Marmousi experience: Velocity model determination on a synthetic complex data set. *The Leading Edge*, 13(9):927–936, 1994.
- J. Virieux and S. Operto. An overview of full-waveform inversion in exploration geophysics. *Geophysics*, 74(6):WCC1–WCC26, 2009.
- J. A. Wade and B. C. MacLean. The geology of the southeastern margin of Canada. In M. J. Keen and G. L. Williams, editors, *Geology of the Continental Margin of Eastern Canada*, volume I-1 of *The Geology of North America (DNAG)*, pages 167–238. Geological Society of America / Geological Survey of Canada, 1990.
- Fu Wang, Xinquan Huang, and Tariq Alkhalifah. A prior regularized full waveform inversion using generative diffusion models. *IEEE Transactions on Geoscience and Remote Sensing*, 61:1–11, 2023a.
- Hongzhou Wang, Jun Lin, Xintong Dong, Shaoping Lu, Yue Li, and Baojun Yang. Seismic velocity inversion transformer. *Geophysics*, 88(4):R513–R533, 2023b.
- Yanghua Wang. The Ricker wavelet and the Lambert W function. *Geophysical Journal International*, 200(1):111–115, 2015.
- Zhou Wang, Alan C. Bovik, Hamid R. Sheikh, and Eero P. Simoncelli. Image quality assessment: From error visibility to structural similarity. *IEEE Transactions on Image Processing*, 13(4):600–612, 2004.
- J. A. W. Weissenberger, R. A. Wierzbicki, and N. J. Harland. Carbonate sequence stratigraphy and petroleum geology of the Jurassic deep Panuke field, offshore Nova Scotia, Canada. In P. M. Harris and L. J. Weber, editors, *Giant Hydrocarbon Reservoirs of the World: From Rocks to Reservoir Characterization and Modeling*, volume 88 of *AAPG Memoir*, pages 395–431. American Association of Petroleum Geologists / SEPM, 2006.
- J. Florian Wellmann, Sam T. Thiele, Mark D. Lindsay, and Mark W. Jessell. pynoddy 1.0: an experimental platform for automated 3-D kinematic and potential field modelling. *Geoscientific Model Development*, 9:1019–1035, 2016.
- Yue Wu and Youzuo Lin. InversionNet: An efficient and accurate data-driven full waveform inversion. *IEEE Transactions on Computational Imaging*, 6:419–433, 2020.
- Fangshu Yang and Jianwei Ma. Deep-learning inversion: A next-generation seismic velocity model building method. *Geophysics*, 84(4):R583–R599, 2019.
- Yan Yang, Angela F. Gao, Jorge C. Castellanos, Zachary E. Ross, Kamyar Azizzadenesheli, and Robert W. Clayton. Seismic wave propagation and inversion with neural operators. *The Seismic Record*, 1(3):126–134, 2021.
- Yan Yang, Angela F. Gao, Kamyar Azizzadenesheli, Robert W. Clayton, and Zachary E. Ross. Rapid seismic waveform modeling and inversion with neural operators. *IEEE Transactions on Geoscience and Remote Sensing*, 61:1–12, 2023.

Gang Yao, Nuno V. da Silva, Michael Warner, Di Wu, and Chenhao Yang. Tackling cycle skipping in full-waveform inversion with intermediate data. *Geophysics*, 84(3):R411–R427, 2019.

Tianze Zhang, Daniel Trad, and Kristopher Innanen. Learning to solve the elastic wave equation with Fourier neural operators. *Geophysics*, 88(3):T101–T119, 2023.

Zhongping Zhang and Youzuo Lin. Data-driven seismic waveform inversion: A study on the robustness and generalization. *IEEE Transactions on Geoscience and Remote Sensing*, 58(10): 6900–6913, 2020.

## A Related Work

We discuss related work along three threads: datasets used to train and evaluate ML-based FWI (Section A.1), machine learning methods for seismic modeling and inversion (Section A.2), and software tools for building velocity models (Section A.3).

### A.1 Datasets for ML-based FWI

Marmousi [Versteeg, 1994, Martin et al., 2006], SEAM [Fehler and Keliher, 2011], OpenFWI [Deng et al., 2022],  $\mathbb{E}^{\text{FWI}}$  [Feng et al., 2023], and GlobalTomo [Li et al., 2025] are well-known datasets for ML-based FWI. Marmousi, SEAM, and OpenFWI are the most closely related to SubsurfaceGen. Each of these datasets falls short on at least one of the four properties from Table 1—field-scale, geologically diverse, physically realistic, extendable—in the following respects:

- **Static datasets.** Existing datasets are fixed collections, which cannot support the experiments required for ML-based FWI to progress. Studying generalization across geological settings, scaling behavior with dataset size, and robustness to distribution shift all require the ability to procedurally generate new data with known properties.
- **Limited spatial extent.** The majority of OpenFWI’s 2D velocity models span only 0.7 km  $\times$  0.7 km. This is problematic because cycle skipping, illumination gaps, and low-frequency recovery all worsen as spatial extent grows: methods evaluated only at small scales provide limited evidence of their performance on real-world surveys.
- **Limited temporal extent.** The majority of OpenFWI’s 2D shot gathers span only 1 s, which limits the maximum imaging depth to the upper 1–2 km of the subsurface, falling well short of the depths where carbon storage sites and hydrocarbons are often found.
- **Limited geological diversity.** Marmousi captures complex folding and faulting, and SEAM captures salt bodies, but neither contains clinoforms, carbonate platforms, or velocity interbedding. OpenFWI’s 2D families lack salt bodies, clinoforms, and velocity interbedding; its 3D family achieves realistic scale (4 km  $\times$  4 km  $\times$  3.5 km, 5 s of recording) but represents a single geological scenario and therefore inherits the same diversity limitations. These omissions correspond to the hardest and most application-relevant regimes of FWI: salt bodies produce strong contrasts that are challenging to invert, carbonate platforms and clinoforms define the sedimentary settings targeted for carbon sequestration and hydrocarbon exploration, and velocity interbedding—thin alternating layers that are difficult to resolve—determines caprock integrity and reservoir quality.
- **Lack of physical realism.** Many of OpenFWI’s 2D velocity models contain visible artifacts that make them physically unrealistic; models trained on them risk learning to reproduce these artifacts rather than geologically meaningful structure.

$\mathbb{E}^{\text{FWI}}$  extends OpenFWI to the elastic wave equation, but inherits OpenFWI’s limited spatial/temporal extent and limited geological diversity. GlobalTomo is intended for whole-Earth seismology (mantle structure, earthquake source mechanics, planetary tomography) rather than the sedimentary settings targeted by SubsurfaceGen.

SubsurfaceGen addresses all of the limitations above, since it enables procedural generation of field-scale, geologically diverse, physically realistic 3D velocity models and seismic data.

## A.2 Machine Learning for Seismic Modeling and Inversion

Wavefield prediction with neural operators [Yang et al., 2021, 2023, Zhang et al., 2023, Huang and Alkhalifah, 2025] has been restricted to small domains (less than one square kilometer) with unrealistic geology (random textures or simple shapes instead of layered, faulted, or salt-containing models) and acquisition geometries unlike real surface surveys (e.g., putting sources on the entire perimeter of the model). SubsurfaceGen provides the data needed to train and evaluate these operators in production-relevant settings, as shown in Section 5. A second line of work learns the inverse map from shot gathers directly to velocity models using neural networks [Araya-Polo et al., 2018, Yang and Ma, 2019, Wu and Lin, 2020, Zhang and Lin, 2020, Wang et al., 2023b]. Jin et al. [2024] scales this approach to 408,000 samples, but is restricted to the small spatial extent of OpenFWI (0.7 km). Only Farris et al. [2023], Farris [2023] has trained end-to-end inversion at field scale—on  $\sim 17 \text{ km} \times 12 \text{ km}$  models in the Gulf of Mexico, using a data engine that was never publicly released. SubsurfaceGen (and the included field-scale dataset) fills this void, and we train inversion baselines on it in Section 6. A third line of work uses generative models trained on velocity models as data-driven priors for FWI [Mosser et al., 2020, Stitt et al., 2023, Wang et al., 2023a, Stitt et al., 2025]; SubsurfaceGen provides a distribution of geologically plausible velocity models required for training these priors.

## A.3 Model Building Tools

Structural geomodeling tools like pynoddy [Wellmann et al., 2016], GemPy [de la Varga et al., 2019], and LoopStructural [Grose et al., 2021] are unable to encode the pixel-level velocity heterogeneity (fractal noise, fine interbedding) that defines the sedimentary basin settings SubsurfaceGen targets. Moreover, they lack a pipeline to generate training data pairs of velocity models and seismic data. The closest peer to SubsurfaceGen is Synthoiseis [Merrifield et al., 2022], a CPU-based pipeline that produces seismic data using 1D reflectivity convolution rather than full wave physics, so the resulting traces lack important phenomena like multipathing and chaotic late-time interference. Synthoiseis also omits modules for realistic salt geometries, carbonate platforms, and clinoforms. SubsurfaceGen closes these gaps: it is GPU-enabled, contains salt, carbonate platform, and clinoform modules, and produces seismic data by solving the acoustic wave equation.

## B Velocity Model Builder: Modules

This appendix gives algorithmic details for the eight builder modules introduced in Section 3 (summarized in Table 5). Each module is described in its own subsection (Sections B.1 to B.8). The companion appendices show how these modules are composed into each geological setting (Section C) and a CPU vs. GPU timing benchmark of the model builder (Section D). **This section leans heavily on geological terminology.**

**Notation.**  $V$  denotes the velocity field  $v_p(\mathbf{x})$  in m/s on a  $(N_z, N_y, N_x)$  grid;  $L$  is an integer-valued volume of the same shape recording which geologic layer each voxel belongs to. The pseudocode below shows updates to  $V$  explicitly; updates to  $L$  happen alongside  $V$  in the implementation but are omitted for clarity. SubsurfaceGen bundles  $V$  and  $L$  in a single data structure.

### B.1 Deposit

The `Deposit` module (Algorithm 1) adds a sedimentary package with interbeds (thin layers of contrasting velocity) on top of a model. Interbed boundaries are 2D surfaces sampled from a 3D simplex noise field (a smooth, spatially correlated random field); each bed is assigned a single Gaussian-drawn velocity with a global depth gradient added across the slab, and an additional 3D simplex noise field provides intra-bed spatial texture (with a per-bed random  $z$ -offset into the shared field decorrelating textures across beds). Layer assignment is vectorized via `torch.searchsorted`. An optional sinusoidal bedform mode (`interbed_mode = "sinusoidal"`) bypasses the boundary-based path and generates the slab as a sum of two sinusoidal harmonics evaluated on a  $z$ -warped axis (depth axis non-uniformly stretched so bed thickness varies; built as the cumsum of a smoothed instantaneous frequency) with added rugosity (small-amplitude roughness), plus an additive 3D patchy-noise texture. Unit convention: the user-facing config specifies  $h$  and  $\sigma_h$  in meters; internally these are divided by the vertical discretization  $\Delta z$  to yield the per-cell quantities used in the formulas below.

Table 5: Catalog of modules in the SubsurfaceGen model builder. Each row describes a module using standard geological terminology.

Module	What it emulates
Deposit	A sediment package laid down between two bedding surfaces, with thickness, base $V_p$ , depth gradient, and interbed reflectivity texture inside.
Squish	Basin-scale vertical warping of all layers above the operator (anticlines, broad post-rift sag) along a single azimuth.
Fault	Applies a localized coordinate warp across a curved fault surface, creating layer offsets and fault-related displacement.
SaltSDT	Inserts one or more irregular high-velocity salt bodies, generated from perturbed 3D ellipsoidal masks.
SaltWedge	The deformation of nearby sediment layers against the flanks of a salt body: layers curving upward against the flank rather than onlapping flat.
CarbonatePlatform	A buried carbonate reef rim with marine-flank, lagoon, and chaotic-core facies, asymmetric along strike.
DeltaClinoformDeposit	Stacks curved clinoform-like bed surfaces to create shelf-to-basin layered geometries with thin internal beds.
StructuralSmoother	Structure-oriented smoothing: anisotropic along bed orientation, weak across bed contacts and fault offsets [Hale, 2009].

---

**Algorithm 1** Deposit.apply (sedimentary package with interbeds)

---

**Require:** Thickness  $t$ , base velocity  $v_0$ , depth gradient  $\beta$ , mean interbed thickness  $\bar{h}$ , interbed-thickness std  $\sigma_h$ , per-bed velocity std  $\sigma_p$ , boundary-noise amplitude  $a_B$ , texture amplitude  $a_\eta$ , taper  $\tau(z) = \min(z/(f_{\text{top}}t), 1) \cdot \min((t-z)/(f_{\text{base}}t), 1)$ .

- 1: Subdivide the slab into  $n \approx \lfloor t/\bar{h} \rfloor$  thin beds: draw thicknesses  $\sim \mathcal{N}(\bar{h}, \sigma_h^2)$  (clamped to  $\geq \frac{1}{2}$  sample), cumsum into internal boundary depths  $\{H_i\}_{i=1}^{n-1}$ .
  - 2:  $H_i(y, x) \leftarrow H_i + \tau(H_i) a_B \eta^{(i)}(y, x)$ , clamped to  $[0, t - 1]$ .
  - 3: Draw per-bed velocities  $v_1, \dots, v_n \sim \mathcal{N}(v_0, \sigma_p^2)$ ; let  $\bar{v} = \frac{1}{n} \sum_\ell v_\ell$ .
  - 4: **for** each voxel  $(z, y, x)$  in the deposit band **do**
  - 5:    $\ell \leftarrow \text{SEARCHSORTED}(\{H_i(y, x)\}, z)$ ;  $S_\ell$  is bed  $\ell$ 's start depth.
  - 6:    $V[z, y, x] = (\bar{v} + \beta z) + \tau(z)[(v_\ell - \bar{v}) + a_\eta \eta_{3D}(z - S_\ell, y, x)]$ .
  - 7: **end for**
  - 8: Per-column sinc-resample  $V$  vertically to conform to the underlying topography  $h(y, x)$ .
- 

## B.2 Squish

The Squish module (Algorithm 2) applies a vertical displacement to a model, emulating basin-scale warping and long-wavelength folding without introducing faulting behavior. The displacement is a 2D fractal noise field with configurable maximum shift, spatial wavelengths, azimuth, and octave count, which is applied to every voxel in the column via sinc resampling.

---

**Algorithm 2** Squish.apply (vertical warping)

---

**Require:** Maximum shift  $\Delta z_{\text{max}}$ , spatial wavelengths  $(\lambda_y, \lambda_x)$ , azimuth  $\alpha$ , octave count  $n_{\text{oct}}$ .

- 1: Sample a 2D fractal-noise displacement field  $\Delta z(y, x)$  with amplitude  $\Delta z_{\text{max}}$ , wavelengths  $(\lambda_y, \lambda_x)$  rotated by  $\alpha$ , summed over  $n_{\text{oct}}$  octaves.
  - 2: Pull-sample  $V$  at  $(z + \Delta z(y, x), y, x)$  via sinc interpolation.
- 

## B.3 Fault

The Fault module (Algorithm 3) applies listric normal-fault deformation to a model. It does this through building a smooth 3D displacement field and then warping the model. Faults are parameterized by a center, azimuth, dip angle, curvature radius, slip magnitude, direction, and die-off

extents. Each voxel in the post-fault model is pull-sampled from its pre-slip position. The fault geometry is represented as a cylindrical coordinate system where a large cylinder radius gives a planar fault while a small radius creates a curved listric fault (l-shaped fault).

Algorithm 3 represents fault slip or displacement as a rotation around this cylinder, with cosine tapers controlling how the displacement dies off across the fault, along strike, and near the ends of the rupture. For each output voxel, the code computes where that voxel came from in the original unfaulted model, then samples the original model at that source location. Continuous fields such as velocity are resampled with sinc interpolation, while integer fields such as layer labels are resampled with nearest-neighbor interpolation. The implementation also supports rough fault surfaces by perturbing the fault radius with fractal noise, and can generate smaller subsidiary faults around a primary fault using simplified Riedel-shear geometry.

---

**Algorithm 3** `Fault.apply` (listric normal-fault deformation, single fault)

---

- Require:** Fault center  $c$ , strike azimuth  $\alpha$ , dip  $\theta$ , curvature radius  $R$ , slip  $s$ , direction  $d \in \{+1, -1\}$ , die-off extents  $(d_{\text{die}}, d_{\text{perp}}, \theta_{\text{die}})$ .
- 1: Cylinder center  $\tilde{c} = c - (\delta_{\text{az}} \sin \alpha, \delta_{\text{az}} \cos \alpha, \delta_z)$  with  $(\delta_z, \delta_{\text{az}}) = (R \sin \theta, R \cos \theta)$ ; reference angle  $\theta_0 = \text{atan2}(\delta_z, \delta_{\text{az}})$ .
  - 2: Slip as rotation:  $\theta_{\text{shift}} = s / (2\pi R) \cdot 360^\circ$ .
  - 3: **for** each voxel  $(z, y, x)$  **do**
  - 4:   Cylindrical coordinates of  $(z, y, x) - \tilde{c}$  in the fault-aligned frame: radius  $r$ , angle  $\theta_{\text{old}}$ , along-strike offset  $\text{az}_{\text{strike}}$ .
  - 5:   Die-off ratios  $\rho_r = |r - R| / d_{\text{die}}$ ,  $\rho_\theta = |\theta_{\text{old}} - \theta_0| / \theta_{\text{die}}$ ,  $\rho_s = |\text{az}_{\text{strike}}| / d_{\text{perp}}$ .
  - 6:   Taper  $w(x) = \cos(\frac{\pi}{2}\rho_r) \cos(\frac{\pi}{2}\rho_\theta) \cos(\frac{\pi}{2}\rho_s) \mathbf{1}\{\rho_r, \rho_\theta, \rho_s < 1\}$ .
  - 7:   Side  $\chi = +1$  if  $r \geq R$  (footwall), else  $\chi = -1$  (hanging wall);  $\theta_{\text{new}} = \theta_{\text{old}} - \chi d w(x) \theta_{\text{shift}}$ .
  - 8:   Forward-mapped position  $p_{\text{fwd}}(z, y, x) \leftarrow$  inverse cylindrical transform of  $(r, \theta_{\text{new}}, \text{az}_{\text{strike}})$ .
  - 9:   Pull source  $\text{src}(z, y, x) = 2(z, y, x) - p_{\text{fwd}}(z, y, x)$  (Cartesian-linearized inverse, exact to first order in  $\theta_{\text{shift}}$ ).
  - 10: **end for**
  - 11: Pull-sample  $V$  at  $\text{src}$  via sinc; voxels with  $\text{src}_z \notin [0, N_z)$  get fill values.
- 

#### B.4 SaltSDT

The `SaltSDT` module (Algorithm 4) generates irregular 3D salt bodies, similar to high-velocity salt structures in the Gulf of Mexico using a signed distance transform perturbed by a Gaussian random field (GRF). Each body starts from a randomly placed and rotated ellipsoid, which provides a simple controllable shape for the salt core. The ellipsoid mask is converted into a signed distance field, so the salt boundary can be modified smoothly by adding a spatially correlated Gaussian random field. The correlation lengths control the preferred scale and direction of boundary variations, while the perturbation amplitude controls how far the final body deviates from the original ellipsoid. Smaller spectral exponents preserve more short-wavelength roughness, whereas larger values produce smoother salt boundaries. After all bodies are generated, their masks are merged, cleaned with morphological opening and closing, and small isolated components are removed. The final mask is prevented from overwriting water and is then assigned the configured salt velocity.

The geometric structure of the salt bodies is controlled by two sets of parameters:  $(\ell_x, \ell_y, \ell_z)$  (anisotropy of the boundary correlation length) and  $(a, p)$  (amplitude and spectral falloff of the perturbation): increasing  $\ell_z$  relative to  $\ell_x$  elongates bodies vertically (as in the Penobscot edge diapir); decreasing  $p$  raises high-frequency roughness on the body boundary; increasing  $a$  pushes bodies further from their base ellipsoid.

#### B.5 SaltWedge

The `SaltWedge` module (Algorithm 5) deforms the sediment column in the neighborhood of salt bodies (produced by `SaltSDT`) to generate flanking onlap and drape geometries consistent with the halokinetic sequence framework of Giles and Rowan [2012]. The goal is not to simulate salt mechanics directly, but to create the common seismic appearance of sediment layers bending, draping, or onlapping near salt bodies. The standard mode computes larger upward shifts near salt and smaller shifts farther away. This shift is strongest near steep salt flanks, decays with distance from the salt,

---

**Algorithm 4** SaltSDT.apply (signed distance transform salt bodies)

**Require:** Body count  $n_b$ , placement bounds, base radius range, anisotropic correlation length fractions  $(f_{\ell_x}, f_{\ell_y}, f_{\ell_z})$ , GRF amplitude  $a$ , spectral exponent  $p$ , salt velocity  $v_s$ , water threshold  $v_{\text{water}}$ .

- 1:  $K \leftarrow \mathbf{0}$ .
- 2: **for**  $i = 1, \dots, n_b$  **do**
- 3:   Sample center, per-axis radii  $(r_x, r_y, r_z)$ , rotation angles; let  $\bar{r} = (r_x + r_y + r_z)/3$ .
- 4:   Rasterize rotated ellipsoid; compute signed distance  $\phi^{(i)}$  via Meijster Euclidean distance transform.
- 5:   Sample GRF  $\xi^{(i)}$  from power spectrum  $P(\mathbf{k}) \propto (1 + \sum_k (k_k \ell_k)^2)^{-p}$  with  $\ell_k = \max(r_k f_{\ell_k}, 5)$ .
- 6:    $\phi'^{(i)}(x) = \phi^{(i)}(x) + a \bar{r} \xi^{(i)}(x)$ ;  $K_i = \mathbf{1}\{\phi'^{(i)} > 0\}$ ;  $K \leftarrow K \vee K_i$ .
- 7: **end for**
- 8: Morphologically open then close  $K$ ; drop connected components smaller than 1000 voxels.
- 9:  $K \leftarrow K \wedge (V \geq v_{\text{water}})$ ;  $V[K] \leftarrow v_s$ .

---

can taper with depth, and is modulated by smooth fractal noise so the deformation is not perfectly symmetric. An optional near-salt squeeze component compresses layers close to the salt flank when its strength is set above zero (off by default). An optional top-conforming mode separately detects the top of the salt body and pushes overlying sediments upward above salt crests, producing diapir-like drape. After the drag, optional squeeze, and optional top-conforming components are combined, the displacement field is clamped to nonnegative values, optionally smoothed in the horizontal plane, made monotone with depth (enabled by default), and then applied as a vertical-only pull warp. Salt voxels themselves are preserved at the configured salt velocity.

---

**Algorithm 5** SaltWedge.apply (sediment deformation around salt bodies)

**Require:** Salt mask  $K$ , base influence  $R_0$ , flank-influence  $R_{\text{flank}}$ , drag exponent  $p$ , vertical-flank threshold  $\tau$ , depth taper  $g(z)$  on  $(z_{\text{top}}, z_{\text{bot}}, g_{\text{pow}})$ , base amplitude  $A_{\text{frac}}$ , conform flag and parameters  $(R_{\text{conform}}, c_{\text{uplift}}, s_{\text{conf}})$ .

- 1: Signed distance  $\phi(x) = d_{\text{out}}(x; K) - d_{\text{in}}(x; K)$ ; vertical normal  $\hat{n}_z = \partial_z \phi / \|\nabla \phi\|$ .
- 2: Vertical-flank set  $V_{\text{flank}} = \{x \in \partial K : |\hat{n}_z(x)| < \tau\}$ ;  $d_{\text{vert}}(x) = \text{EDT distance to } V_{\text{flank}}$ .
- 3: Drag weights  $w_d(x) = (\max(0, 1 - \phi/R_{\text{field}}(z)))^p$ ,  $w_v(x) = \exp(-(d_{\text{vert}}/R_{\text{flank}})^2)$ ,  $w = w_d w_v \mathbf{1}\{x \notin K\}$ , with  $R_{\text{field}}(z) = R_0(1 + \beta_{\text{rad}} \sin(\pi z/N_z))$ .
- 4: Drag displacement  $\Delta z_{\text{drag}}(x) = A_{\text{frac}} N_z w(x) g(z) A(x)$ , with  $A(x)$  a fractal amplitude field.
- 5: **if** conform enabled **then**
- 6:   Salt-top  $\zeta_{\text{top}}(y, x) = \min\{z : K[z, y, x] = 1\}$ ; crest relief  $R_{\text{crest}} = \max(0, \text{Gauss}_\sigma(\zeta_{\text{top}}) - \zeta_{\text{top}})$ , normalized to  $[0, 1]$ .
- 7:    $\Delta z_{\text{conf}}(x) = c_{\text{uplift}} N_z s_{\text{conf}} R_{\text{crest}}(y, x) e^{-(\zeta_{\text{top}} - z)/R_{\text{conform}}} g(z) \mathbf{1}\{z < \zeta_{\text{top}}, x \notin K\}$ .
- 8: **else**
- 9:    $\Delta z_{\text{conf}} \leftarrow 0$ .
- 10: **end if**
- 11:  $\Delta z(x) = \max(0, \Delta z_{\text{drag}} + \Delta z_{\text{conf}})$ ; enforce monotonicity  $\Delta z[z, y, x] \leftarrow \max_{z' \leq z} \Delta z[z', y, x]$ .
- 12: Warp  $V$  by pull-sampling at  $(z + \Delta z, y, x)$  with  $z$ -linear interpolation; salt voxels held at  $v_s$ .

---

## B.6 CarbonatePlatform

The CarbonatePlatform module (Algorithm 6) builds asymmetric reef bodies with a steep marine flank, a gentle leeward ramp, and a “chaotic” core. Multiple platforms along a shared strike direction are merged via a smooth-minimum signed distance operator with a configurable blending parameter. Facies velocities (core, marine forereef, lagoon, carbonate basin, sequence boundary) are assigned separately. A lateral fill texture with interbedded velocities and a patchy 3D noise field fills the surrounding sediment bounded by the platform contacts.

---

**Algorithm 6** CarbonatePlatform.apply (asymmetric reef body with facies zoning)

**Require:** Thickness  $t_{\text{use}}$ , platform azimuth  $\alpha$ , center count  $N_p$ , width fraction  $f_w$ , shape exponent  $\kappa$ , marine squash  $\mu$ , leeward stretch  $\lambda$ , growth phases  $n_{\text{phases}}$ , smooth-min parameter  $k$ , facies velocities, lateral-fill fraction  $f_{\text{fill}}$ .

- 1: Domain-warp the horizontal grid:  $(y_w, x_w) = (y, x) + a_w(\eta_y, \eta_x)$ .
  - 2: Sample  $N_p$  platform-center paths  $(c_y^{(j)}(t), c_x^{(j)}(t))$  as oscillation + smoothed walk + drift along  $\alpha$ .
  - 3: For each platform  $j$ : rotate into marine-strike frame, split marine vs leeward by  $\mu, \lambda$ , and form normalized distance  $\text{dist}_j(y, x) = \sqrt{(d_{\text{mar}}^{\text{asym}})^2 + d_{\text{str}}^2 / r_{\text{eff}}^{(j)}}$ .
  - 4: Blend platforms via smooth-minimum:  $\text{dist}_{\text{blend}} = \text{smin}_k(\text{dist}_1, \dots, \text{dist}_{N_p})$ .
  - 5: Build 2D thickness map  $T(y, x)$  from  $n_{\text{phases}}$  growth lenses  $\exp(-\text{dist}_{\text{blend}}^\kappa)$ , normalized to  $[\text{min\_frac}, 1] t_{\text{use}}$ .
  - 6: Build unmorphed volume of shape  $m_{\text{mound}} \times N_y \times N_x$ : assign facies velocity from  $\{v_{\text{core}}, v_{\text{fore}}, v_{\text{lag}}, v_{\text{basin}}\}$  via  $(\text{dist}_{\text{blend}}, \text{bias})$  where  $\text{bias}_j = \frac{1}{2}(d_{\text{mar}}/|d| + 1)$  marks each voxel marine-vs-leeward; add  $n_{\text{ib}}$  interbeds and core texture.
  - 7: Per-column linearly resample to  $T(y, x)$  samples and place into  $z \in [h - T, h)$ .
  - 8: Off-platform columns in  $[h - f_{\text{fill}} t_{\text{use}}, h)$  get a low-velocity interbed fill.
- 

**B.7** DeltaClinoformDeposit

The DeltaClinoformDeposit module (Algorithm 7) generates forestepping deltaic packages as a stack of flat  $N_c$  clinothem envelopes, each containing  $B$  internal beds. Internal beds are then created by interpolating between the previous surface and the clinothem envelope, producing thin layers that follow the same folded-over clinoform geometry. The module can optionally vary the rollover position, extent, truncation, and onlap taper from one clinothem to the next using a prescribed sequence of systems-tract labels, but these labels act only as geometric controls on the stacked surfaces rather than as a full process-based depositional model.

---

**Algorithm 7** DeltaClinoformDeposit.apply (forestepping clinothem package)

**Require:** Basinward azimuth  $\alpha$ , clinothem count  $N_c$ , beds per clinothem  $B$ , envelope sharpness  $(s_{\text{fore}}, s_{\text{toe}})$ , flat-topset fraction  $\phi_{\text{flat}}$ , toe parameters  $(u_{t,0}, d_{\text{toe}}, \beta_{\text{toe}})$ , rollover advance  $\Delta u_r$ , optional systems-tract sequence, lobe shape, facies velocities, truncation period  $n_{\text{trunc}}$ . Let  $\sigma(x) = 1/(1 + e^{-x})$ ; rotated  $(u, v)$  coordinates with  $u \in [0, 1]$  landward→basinward.

- 1: **for**  $k = 1, \dots, N_c$  **do**
  - 2:     Update rollover  $u_{r,k} = u_{r,0} + R_k$  with cumulative advance  $R_k = R_{k-1} + \Delta r_k$  (per-tract sign).
  - 3:     Lobe taper  $\Lambda(y, x)$ : super-Gaussian in across-strike coordinate  $v$ .
  - 4:     Envelope (two-stage composition): main foreset  $z_{\text{main}}(u) = z_k^{\text{top}} + (z_k^{\text{fore}} - z_k^{\text{top}}) \sigma(s_{\text{fore}}(u_{\text{eff}} - u'_{r,k}))$ ; toe stage  $z_{\text{env}}(u) = z_{\text{main}} + (z_{\text{toe}}^* - z_{\text{main}}) \sigma(s_{\text{toe}}(u - u_{t,0})) \beta_{\text{toe}}$ .
  - 5:     **for**  $b = 1, \dots, B$  **do**
  - 6:         Bed surface  $z_{k,b} = z_{k,\text{base}} + (z_{\text{env}} - z_{k,\text{base}})(b/B) \Pi(u) \Lambda(y, x)$ , where  $z_{k,\text{base}}$  is the base of clinothem  $k$  (the top of clinothem  $k-1$ ) and  $\Pi(u)$  is a product of  $\sigma$ -gated onlap, extent, and shift tapers.
  - 7:         Bed velocity  $v_b = v_{\text{base}} + v_{\text{range}}(f - 0.5) \cdot 2 + a_{\text{lam}}(-1)^{kB+b} + \gamma z_{k,b}$ , where  $f$  is the  $\sigma$ -blended sand fraction across topset/foreset/toe zones.
  - 8:     **end for**
  - 9:     **if**  $k \bmod n_{\text{trunc}} = 0$  **then**
  - 10:         Erode the top  $\min(B, k)$  bed surfaces toward the stack surface (toplap sequence boundary).
  - 11:     **end if**
  - 12: **end for**
  - 13: Rasterize via soft-Heaviside anti-aliasing over all  $N_c B$  bed surfaces.
-

## B.8 StructuralSmoother

The `StructuralSmoother` module (Algorithm 8) implements structure-oriented smoothing [Hale, 2009]. The goal is to smooth the velocity volume anisotropically: strongly along the local bed direction, weakly across it. The operator estimates local orientation from a structure tensor built from Sobel-filtered gradients of  $V$ , then computes an eigendecomposition of the smoothed structure tensor to construct a per-voxel diffusion tensor. The smoothed output is the solution of a symmetric positive-definite linear system solved by conjugate gradient.

---

### Algorithm 8 `StructuralSmoother.apply` (Structure-oriented smoothing)

---

**Require:** Tensor-smoothing scale  $\sigma_{\text{tensor}}$ , multi-scale window  $W$ , smoothing scale  $c$ , cross-layer diffusivity  $\alpha \in (0, 1]$ , conjugate gradient iteration budget  $n_{\text{cg}}$ .

- 1: Structure tensor  $T(x) = \sum_{s=1}^W \frac{1}{s} g_s(x) g_s(x)^\top$  with  $g_s = \nabla V$  at scale  $s$ ; Gaussian-smooth each component at scale  $\sigma_{\text{tensor}}$ .
  - 2: Eigendecompose  $T$  pointwise into  $\lambda_u \geq \lambda_v \geq \lambda_w$  with eigenvectors  $u, v, w$ ; build diffusion tensor  $D(x) = \alpha uu^\top + vv^\top + ww^\top$ .
  - 3: Solve  $(I + cG^\top DG)y = V$  by  $n_{\text{cg}}$  conjugate gradient iterations, where  $G$  is the discrete 3D gradient operator.
- 

## C Velocity Model Builder: Model Generation for Field-Scale Dataset

This appendix describes the model building process for the six geological settings in our field-scale dataset on Hugging Face. For each setting we give (i) a description of the model, (ii) the real-world geological settings that inspired it (with supporting references), (iii) the module builder sequence with module configurations, and (iv) what geological features we deliberately leave out. The modules are in Section B; CPU vs. GPU timings for the model builder are in Section D. **This section leans heavily on geological terminology.**

Every velocity model has shape  $619 \times 1000 \times 1000$  at 10 m isotropic spacing. Table 6 gives the full inventory and Fig. 8 provides build scripts and visualizations of models and migrated cubes for the Penobscot and F3 settings.

Table 6: Velocity model inventory. The velocity models all have identical shape and are at 10 m resolution. Penobscot is held out as the out-of-distribution test set during training; the remaining 41 models populate training and in-distribution test splits.

Name	Volumes	Shipped shape	Setting
F3	10	$619 \times 1000 \times 1000$	Dutch North Sea, deltaic shelf with deep salt
GoM	10	$619 \times 1000 \times 1000$	Gulf of Mexico, allochthonous salt bodies
Fault	5	$619 \times 1000 \times 1000$	Dense normal-fault basin (stress test)
Salt Canopy	4	$619 \times 1000 \times 1000$	Gulf of Mexico, tabular salt canopy
SEAM (Phase I)	12	$619 \times 1000 \times 1000$	Deepwater GoM, reused industry model
Penobscot (OOD)	1	$619 \times 1000 \times 1000$	Scotian Shelf, carbonate platform

### C.1 Penobscot

Our Penobscot model is a thick carbonate platform at depth, overlain by a siliciclastic column with a main listric fault and a small salt diapir at one edge. The setting is the LaHave Platform on the Scotian Shelf (offshore Nova Scotia): a Mesozoic passive margin that accumulated kilometers of post-rift sediment over a Late Jurassic carbonate bank [Wade and MacLean, 1990, Brown, 2008]. The Abenaki Formation is the geologic anchor [Eliuk, 1978, Weissenberger et al., 2006]. The Penobscot 3D survey itself is contributed by CNSOPB and dGB Earth Sciences [Baroni et al., 2019]. The field has no thick allochthonous salt the way the Gulf of Mexico does; its salt contribution is subordinate and mostly confined to the adjacent Sable Subbasin [Kidston et al., 2002, Brown, 2008]. We create a minor diapir in the synthetic to add some halokinetic texture in an otherwise salt-poor geology.

The builder runs a deterministic 21 step sequence on a  $1000 \times 1000$  grid at 10 m isotropic spacing. It lays a 5500 m/s basement and a 30 cell pre-carbonate at 4000 m/s with sinusoidal interbeds. The

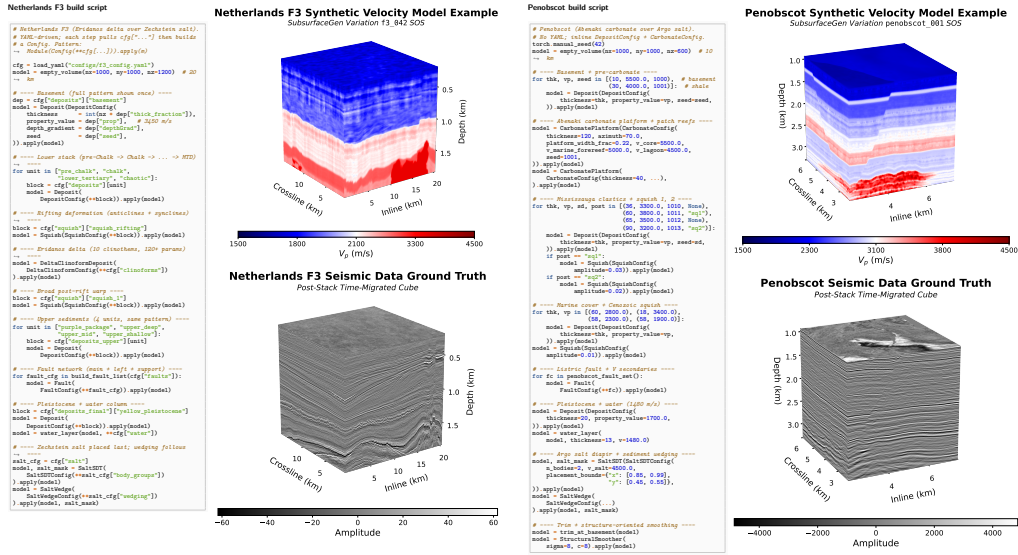


Figure 8: Python build scripts and (velocity model, migrated cube) pairs for Penobscot (left) and F3 (right). Each build script is a sequence of `Module(Config(...)).apply(model)` calls that create geological features in the velocity model. Each call corresponds to a feature visible in the migrated cube, e.g., the carbonate platform in Penobscot and the clinothem stack and salt diapir in F3.

carbonate is added via two `CarbonatePlatform` passes: a 120 cell main platform with three lateral platform centers (core 5500, forereef 5000, lagoon 4200, carbonate basin 3500 m/s) and a 40 cell patch-reef pass with four smaller reef bodies. A 36 cell basin-fill deposit at 3300 m/s drapes the carbonate flanks. Seven `Deposit` events then reproduce the clastic overburden in stratigraphic order from Lower Mississauga (3800 m/s) up through Banquereau Upper (1900 m/s), with a thin Wyandot chalk unit (3400 m/s, suppressed interbed taper) embedded in the middle. A final 20 cell shallow Pleistocene deposit at 1700 m/s drapes the faulted surface before the water column. Three `Squish` events apply basin-scale vertical warping at decreasing amplitude (90, 65, 40 m). One listric main fault (azimuth  $50^\circ$ , dip  $30^\circ$ , slip fraction 0.025) and four V-shaped secondaries (paired at  $25^\circ$  and  $155^\circ$  around common centers) give a total of five fault events. A two-body salt diapir is placed on the right edge (placement bounds  $x \in [0.84, 0.98]$ ), vertically elongated (correlation anisotropy [1.5, 0.6, 0.6]), and flanked by the `SaltWedge` module. A 13 cell water column at 1480 m/s caps the model.

What is real: the carbonate-clastic contrast, the five faults, the small-edge diapir, and the broad basin-warping sequence. What we skip: the specific Abenaki reef-margin mode (rimmed-shelf versus barrier-bank) and the Penobscot Canyon erosional feature.

## C.2 F3

Our F3 model is a deltaic-shelf model with deep salt and large-scale faulting. The reference is the F3 Block in the Dutch sector of the Central Graben, an open 3D seismic volume widely used in seismic interpretation [Silva et al.]. Two features drive the modeling choices. First, Permian-age salt (the Zechstein) sits at depth and acts as a weak layer: sediment loading above it generates large-scale faults that sole into the salt rather than into the underlying brittle basement [Davison et al., 2000]. Second, the Plio-Pleistocene section records the Eridanos river system, a continental-scale delta that drained northwestern Europe into the southern North Sea and left behind repeated basinward-stepping clinothem packages (a clinothem is one dipping shelf-slope-basin sediment body) [Overeem et al., 2001, Kuhlmann et al., 2006].

Build-time grid is  $1000 \times 1000 \times 1200$  at 20 m horizontal and 2.5 m vertical spacing; the shipped volumes resample to a  $619 \times 1000 \times 1000$  grid at 10 m resolution. The stratigraphy is built deep to

shallow: a 3450 m/s basement, a pre-chalk Scruff analogue (2600 m/s), a Chalk unit with the lowest interbed contrast in the model (2900 m/s, 40 m/s std), a Lower Tertiary package (2200 m/s), and a chaotic mass-transport layer (2300 m/s, 250 m/s std: the *highest* interbed contrast in the model). A rifting-phase squish (75 m max shift at 90° azimuth) warps the pre-cliniform section. The delta itself is built by the `DeltaClinoformDeposit` module: ten forestepping clinothems (range 8–12 per realization), twelve beds each on average, stacked along a 133° SE trajectory with a rollover at 18 % along the profile, a flat topset fraction of 0.5, and a toe-flattening strength of 0.75. A second broad squish (35 m max shift, near-zero azimuth) warps the pre-salt section before upper deposits are applied. Four shallower deposits (Purple 1925, Upper Deep 1850, Upper Mid 1800, Upper Shallow 1750 m/s) overlie the delta. One main long-wavelength fault (azimuth 145°, dip 30°), a left-side fault cluster of ~14 faults, and 2–4 geologically-placed support faults (offset from the main fault by +15° and +165°, 60/40 split) reproduce the F3 fault population. A Yellow-Pleistocene cap at 1650 m/s drapes the faulted surface, and a 30 cell water column at 1500 m/s tops the model. Five salt-body groups (three on a diagonal chain, two outskirt) are placed below  $z = 0.40 \cdot n_z$  at 3500 m/s, then draped by a surface-conforming `SaltWedge` pass.

We refer to the shelf-slope-basin geometry as *oblique-tangential* using the seismic-stratigraphy vocabulary of Mitchum et al. [1977], and describe the stacking pattern as *forestepping* or via the shelf-edge-trajectory language of Helland-Hansen and Hampson [2009]. The word “progradation” describes a temporal depositional process; our model is a static velocity volume, so the geometric terms fit better.

What is real: the clinothem geometry, the Zechstein-decoupled fault style, and the deep-to-shallow velocity trend. What we skip: intra-clinothem mass-transport deposits, salt-pillar welding into the Jurassic section, and glaciomarine fabrics in the uppermost Pleistocene.

### C.3 Fault

The Fault setting is a stress test, not a field. It gives the training set dense normal-fault populations with high velocity contrast across sub-parallel fault arrays. The closest natural analogue is the post-rift section of the North Sea (Viking and Central Graben), where two superposed Mesozoic rifting phases left a multi-orientation normal-fault population with widespread block rotation [Badley et al., 1988, Underhill and Partington, 1993]. We reference the fault-population literature for the mechanism by which primary faults seed sub-seismic secondaries: displacement-length scaling [Cowie and Scholz, 1992], 3D fault-surface geometry [Nicol et al., 1996], relay-ramp breaching between overstepping segments [Peacock and Sanderson, 1994], and along-strike displacement patterns from the East African Rift [Morley, 1999]. The integrating tectono-sedimentary framework is described in Gawthorpe and Leeder [2000].

The builder stacks four contrast-producing deposits on a 5000 m/s basement (Fig. 9): deep 4000 m/s, mid 3200 m/s, upper 2500 m/s, and a post-fault drape at 1950 m/s. Two squish events interrupt the stack (200 m and 130 m max shift). Each realization then draws 3, 4, 5, or 6 primary faults from an inclusive integer range; primary count is *not* fixed. All primaries share one system azimuth drawn from  $[-45^\circ, +45^\circ]$ , are confined to non-crossing lanes perpendicular to that azimuth, and carry the same slip direction so the array reads as a single sub-parallel population. Per primary, 20–30 secondary faults are generated using Riedel-shear geometry: synthetic R-shears offset by +15° from the primary, antithetic R'-shears by +165°, with 85 % synthetic bias and a 0.75 hanging-wall placement bias. A minimum-distance filter rejects overlapping subsidiaries, so the post-filter secondary count varies with realization. After faulting, a drape deposit heals the discontinuity-bearing surface, a 15 cell water column at 1480 m/s goes on top, and the final clamp to [1500, 5000] m/s removes any outliers introduced by fault-zone interpolation.

What is real: the primary-array style, the Riedel-geometry secondary pattern, and the high-contrast deposit stack. What we skip: overpressure-driven polygonal faulting, fault-zone damage halos, and listric detachment into a ductile basal layer. These realizations push the wavefield operator against dense discontinuities, not against the mechanical specifics of any named rift system.

### C.4 Gulf of Mexico

Our GoM analogue is a deepwater salt-tectonics model: multiple salt bodies embedded in a layered sediment column, with sediments deformed upward against salt flanks. The setting is the northern

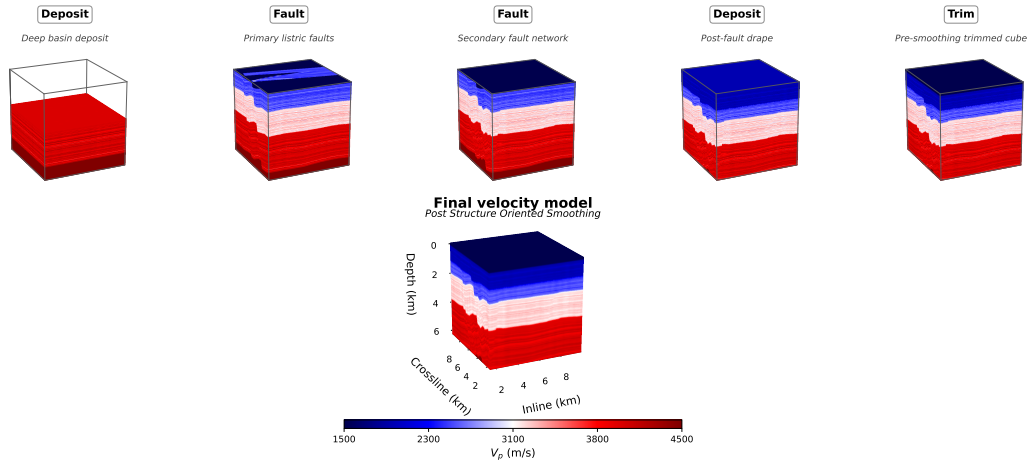


Figure 9: Per-stage build of one realization of the Fault setting. Reading left-to-right, top-to-bottom: the basement (5000 m/s) is laid down, followed by the four contrast-producing deposits (4000, 3200, 2500 m/s and the post-fault drape at 1950 m/s) interleaved with two squish events that warp the lower stack. The drape deposit then heals the discontinuity-bearing surface and the water column caps the model.

Gulf of Mexico passive margin, where salt from a deep Jurassic source layer has risen through the overlying sediment as walls, stocks, sheets, and coalesced canopies [Diegel et al., 1995, Peel et al., 1995, Hudec et al., 2013]. *Allochthonous* means that the salt has been transported out of its original stratigraphic position, leaving behind sediment-filled *minibasins* between the new salt bodies. These minibasins form because sediment loading differentially depresses the surrounding salt [Hudec and Jackson, 2007]. The rise of a salt diapir also deforms the flanking sediments, producing thinned and folded packages whose geometry is formalized as *halokinetic sequences* (narrow hook sequences when the diapir rises fast relative to sedimentation, broad wedge sequences when it rises slowly) [Giles and Rowan, 2012]. The geometric consequence for imaging is a large sediment-to-salt velocity jump that produces shadow zones and multipathing in ray-based tomography [Sava and Biondi, 2004a,b, Jones and Davison, 2014, Jackson and Hudec, 2017].

The builder runs on a  $1000 \times 1000 \times 800$  grid at 10 m resolution. A 5 cell 4500 m/s basement is overlain by nine Deposit events (Fig. 10) with base velocities decreasing upward from 2900 m/s (deep Lower Tertiary) to 1800 m/s (Pleistocene). Five squish events interleave with the deposits; squish amplitude decreases upsection from 500 m to 100 m, giving the kind of depth-dependent folding one expects when older sediment has seen more deformation. The SaltSDT module inserts 2–7 salt bodies per realization (base 4) at 4500 m/s, placed at depth fractions [0.15, 0.60], with a correlation length of 0.7 in each axis on the GRF perturbing the body boundary. The SaltWedge module then deforms the surrounding sediment with a combination of a Gaussian weight in distance to the nearest vertical flank, a radial drag weight raised to the 1.8 power, a depth-dependent taper, and a fractal spatial-amplitude field. The net effect curves sediment upward against salt flanks and drapes it onto salt roofs, which is the geometric shape that the tapered (wedge) class of halokinetic sequence produces [Giles and Rowan, 2012]. A 96 cell water column at 1500 m/s caps the column.

What is real: the  $\sim 2700$  m/s salt-to-sediment velocity jump, the variety of individual salt-body shapes that a parametric perturbation can span, and the upward-flanking sediment geometry. What we skip: welded or rafted salt architectures, dissolution textures, and multi-stage salt-tectonic histories.

## C.5 Salt Canopy

The Salt Canopy model represents a second GoM setting. Multiple allochthonous salt sheets have coalesced laterally into a shallow, approximately tabular body above interbedded sediments. Unlike the diapir-dominated GoM setting above, the canopy is continuous in map view and produces the canonical subsalt imaging problem [Hudec and Jackson, 2006, Pilcher et al., 2011, Jones and Davison,

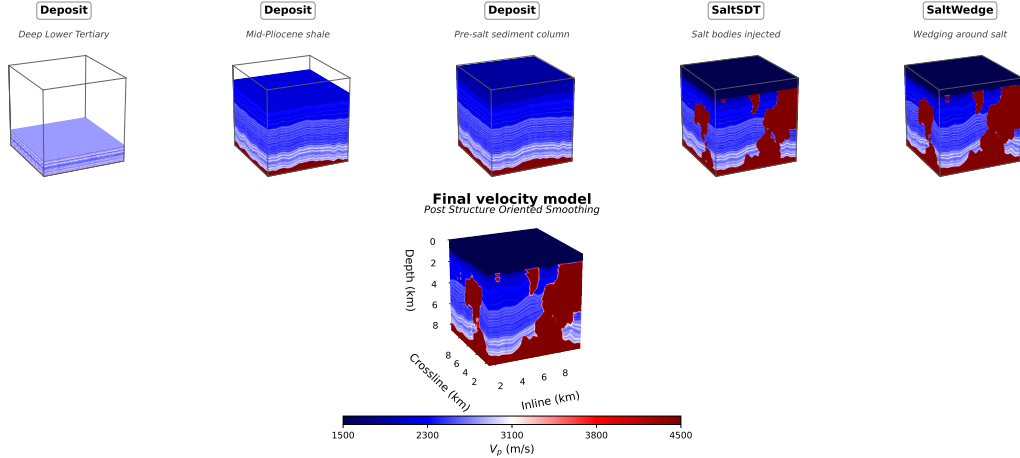


Figure 10: Per-stage build of one realization of the Gulf of Mexico setting. Reading left-to-right, top-to-bottom: the 5 cell basement (4500 m/s) is overlain by nine sediment deposits whose base velocities decrease upward (Lower Tertiary 2900 m/s through Pleistocene 1800 m/s), with five squish events of decreasing amplitude (500, 400, 300, 200, 100 m) interleaved between specific deposits to produce depth-dependent folding. The salt stage inserts SDT-generated bodies at depth fractions [0.15, 0.60], and the wedging stage deforms the surrounding sediment to produce the upward onlap and drape characteristic of halokinetic sequences.

2014, Sava and Biondi, 2004b]. The BP-operated Tiber discovery in Keathley Canyon block 102 is a widely cited field example of canopy salt.

The four canopy models in the dataset predate the SaltSDT module and were built with a legacy code path (`pysaltmodel`) on a  $1584 \times 2096 \times 536$  generation grid at 10 m resolution, then resampled and depth-truncated to the common  $619 \times 1000 \times 1000$  grid. Each salt body is the volume between two 2D fractal-noise elevation surfaces (a “top” and a “bot”) filled at salt velocity, with a frequency-octave ladder of [2, 4, 8, 16, 32] and an amplitude ladder of [1, 0.3, 0.1, 0.05, 0.025]. Sediment is filled both below and above the salt regime. A correction pipeline then inpaints low-velocity voxels, caps velocities at 5000 m/s, cuts below a detected basement, adds a  $130 \pm 10$ -cell water column at 1500 m/s, and clamps the final volume to [1500, 5000] m/s. This model building process is inspired by Farris et al. [2023], Farris [2023].

What is real: the tabular canopy morphology and the subsalt sediment–salt–sediment contrast. What we skip: inter-canopy saline-entrainment textures and sub-canopy overpressure signatures mapped in the real-world Keathley Canyon section.

## C.6 SEAM Phase I

The twelve SEAM models are *reused, not generated*. They come from the SEG Advanced Modeling (SEAM) Phase I 3D earth model [Fehler and Keliher, 2011], which was built by an industry consortium between 2007 and 2013 to model a salt canopy region of the deepwater Gulf of Mexico. We incorporate SEAM because it is a community-validated reference model in the same regime as our Salt Canopy setting. The Phase I model is distributed under CC BY 4.0 through the SEG SEAM Open Data program [Society of Exploration Geophysicists, 2024].

The raw Phase I model is  $1501 \times 4001 \times 3501$  at 10 m resolution (15 km  $\times$  40 km  $\times$  35 km). Our pipeline extracts twelve  $1501 \times 1000 \times 1000$  subregions on a  $4 \times 3$  grid. We apply structure-oriented smoothing to each subregion ( $\sigma_{\text{tensor}} = 8$  cells, smoothing-scale = 8 cells,  $\alpha = 0.3$ , 10 conjugate gradient iterations) and clamp to [1500, 5000] m/s. Each subregion is depth-truncated to 619 cells, which is followed by structure-oriented smoothing with  $\sigma_{\text{tensor}} = 8$ , smoothing-scale = 8,  $\alpha = 0.3$ , and 10 conjugate gradient iterations.

What is real: SEAM is based on real-world geology. What we skip: N/A.

## D Velocity Model Builder: GPU vs. CPU Timing

This appendix backs Table 2 with hardware, methodology, per-stage timings, and per-module timing totals. The modules are described in Section B; the per-setting build sequences are in Section C.

**Hardware.** A single compute node with one 80 GB A100 NVIDIA GPU and an AMD EPYC 7763 host (16-core / 256 GB allocation). The GPU was held in CUDA Exclusive\_Process mode so no other process contended for the device. CPU runs set `CUDA_VISIBLE_DEVICES=""` to avoid creating a CUDA context, with BLAS / OpenMP thread counts pinned to 16.

**Methodology.** Each (setting, device) pair runs as a new Python subprocess. Per-stage timings use `time.perf_counter()` bracketed by `torch.cuda.synchronize()` on the GPU run. GPU utilization and memory usage are sampled 10 times per second, i.e., at 10 Hz.

**Per-setting totals.** Table 7 stacks the wall-time breakdown alongside peak GPU memory and peak CPU memory. Wall is the full subprocess time including Taichi initialization, CUDA-context setup, and inter-stage cleanup; the gap between Wall and Build is the warm-up plus Python overhead.

Table 7: Per-setting totals. Build is the sum of per-stage build times. Wall is the full subprocess wall time. Peak GPU (CPU)memory is the maximum GPU (CPU) memory used during the run.

Setting	Stages	GPU build (min)	GPU wall (min)	Peak GPU memory (GB)	CPU build (min)	CPU wall (min)	Peak CPU memory (GB)
Penobscot	21	5.57	6.66	48.6	92.67	92.72	74.2
F3	15	11.49	12.60	60.0	82.29	82.46	137.4
Fault	12	5.84	6.56	67.7	156.57	156.69	68.0
GoM	19	6.70	7.84	52.3	100.21	100.31	92.8

**Per-stage breakdowns.** Tables 8 to 11 list every module call. `canonical_sos` is the final `StructuralSmoother` call; the four water stages set the water column velocity and run in milliseconds on both CPU and GPU.

Table 8: Per-stage build for the Penobscot setting. Speedup is the ratio of CPU to GPU build time. Avg / pk util are weighted-average and peak GPU utilization sampled at 10 Hz across the stage. Pk CPU memory is the maximum sampled CPU memory usage.

#	Stage	GPU s build	CPU s build	Speedup	Pk GPU memory (GB)	Avg util %	Pk util %	Pk CPU memory (GB)
1	basement	0.003	0.033	10.77x	0.08	0.0	0	0.58
2	pre_carbonate	0.822	2.924	3.55x	8.55	2.2	14	8.98
3	abenaki_carbonate	2.765	85.426	30.90x	10.32	38.1	100	11.01
4	basin_fill	26.330	500.397	19.00x	21.53	61.2	69	22.20
5	lower_mississauga	20.395	389.918	19.12x	21.34	65.1	74	22.03
6	squish_basin_subsidence	0.732	14.626	19.98x	11.48	6.6	53	9.41
7	upper_mississauga	22.446	443.507	19.76x	23.92	64.9	100	24.63
8	logan_canyon	33.688	684.111	20.31x	25.65	66.8	73	26.35
9	squish_mid_cret	0.616	19.470	31.63x	17.62	24.6	43	14.55
10	dawson_canyon	16.508	330.979	20.05x	27.04	66.9	75	27.76
11	wyandot_chalk	4.055	84.690	20.88x	15.57	60.0	73	16.12
12	banquereau_lower	18.614	381.580	20.50x	26.97	67.8	76	27.65
13	banquereau_upper	17.934	347.060	19.35x	28.13	65.6	82	28.85
14	squish_cenozoic	1.012	26.957	26.64x	25.13	29.0	44	20.55
15	faults	26.256	990.567	37.73x	48.56	90.8	100	39.29
16	final_deposit	7.229	150.028	20.76x	21.52	64.5	75	22.00
17	water	0.000	0.004	7.95x	5.49	0.0	0	0.00
18	salt	34.370	33.035	0.96x	14.71	0.6	15	15.91
19	wedging	76.354	75.358	0.99x	30.84	2.4	100	74.18
20	trim	0.159	1.283	8.08x	17.82	0.0	0	18.67
21	canonical_sos	24.097	998.233	41.42x	40.35	95.0	100	49.73
Total		334.38	5560.18	16.63x	48.56	47.7	100	74.18

**Per-module totals and observations.** Table 12 groups the per-stage rows by builder module. The largest speedups are on Fault (38.9 $\times$ ) and `StructuralSmoother` (34.5 $\times$ ). Deposit has a smaller

Table 9: Per-stage build for the F3 setting. Speedup is the ratio of CPU to GPU build time. Avg / pk util are weighted-average and peak GPU utilization sampled at 10 Hz across the stage. Pk CPU memory is the maximum sampled CPU memory usage.

#	Stage	GPU s build	CPU s build	Speedup	Pk GPU memory (GB)	Avg util %	Pk util %	Pk CPU memory (GB)
1	basement	0.170	0.017	0.10x	0.03	0.0	0	0.00
2	pre_chalk	47.365	270.485	5.71x	19.95	65.9	100	20.22
3	chalk	18.233	98.506	5.40x	21.57	59.9	90	21.73
4	lower_tertiary	36.707	210.725	5.74x	24.27	69.2	74	24.54
5	chaotic	28.003	146.240	5.22x	25.81	66.8	74	25.62
6	squish_rifting	0.846	11.690	13.82x	18.61	7.5	12	15.03
7	clinoforms	28.218	360.272	12.77x	14.81	73.3	100	15.65
8	squish	0.960	15.206	15.84x	23.76	47.6	100	19.43
9	upper_deposits	78.208	427.135	5.46x	36.36	70.5	100	36.62
10	faults	73.570	1907.790	25.93x	57.10	89.4	100	53.03
11	final_deposit	25.849	143.507	5.55x	36.92	69.4	81	36.89
12	water	0.001	0.006	7.41x	8.64	0.0	0	0.00
13	salt	239.939	190.560	0.79x	27.43	0.9	78	33.18
14	wedging	73.038	81.806	1.12x	44.53	2.9	100	137.43
15	canonical_sos	38.288	1073.629	28.04x	60.00	95.0	100	108.32
Total		689.40	4937.57	7.16x	60.00	41.6	100	137.43

Table 10: Per-stage build for the Fault setting. Speedup is the ratio of CPU to GPU build time. Avg / pk util are weighted-average and peak GPU utilization sampled at 10 Hz across the stage. Pk CPU memory is the maximum sampled CPU memory usage.

#	Stage	GPU s build	CPU s build	Speedup	Pk GPU memory (GB)	Avg util %	Pk util %	Pk CPU memory (GB)
1	basement	0.004	0.091	22.48x	0.80	5.0	5	0.00
2	deep_deposit	68.242	773.786	11.34x	23.61	66.0	71	23.85
3	squish_deep	1.011	12.458	12.32x	14.03	1.8	3	11.65
4	mid_deposit	49.081	404.522	8.24x	27.47	71.1	100	27.88
5	squish_shallow	0.977	17.346	17.75x	20.82	0.0	0	16.82
6	upper_deposit	30.110	243.264	8.08x	30.08	69.4	99	30.75
7	primary_faults	49.585	1837.841	37.06x	67.67	97.1	100	53.36
8	secondary_faults	91.252	4636.105	50.81x	55.20	72.1	100	56.01
9	post_fault_drape	37.125	730.076	19.67x	37.80	67.6	75	38.40
10	water	0.001	0.010	10.09x	8.99	0.0	0	0.00
11	trim_clamp	0.128	2.369	18.53x	21.70	0.0	0	22.12
12	canonical_sos	23.130	736.401	31.84x	41.55	95.7	100	68.04
Total		350.64	9394.27	26.79x	67.67	74.7	100	68.04

per-call speedup (13.6 $\times$ ) but its high call count makes it the biggest contributor to total time saved. SaltSDT and SaltWedge show no GPU advantage; improving these implementations is a target for future work.

## E Seismic Forward Modeling Details

This appendix gives slice extraction, numerical scheme, source wavelet, and acquisition geometry details for the seismic data generation in Section 4.

### E.1 Slice extraction and dataset organization

The 2D dataset is produced from the 42 3D volumes (Table 6) by a deterministic extractor with seed 42. All volumes are first depth-truncated to 619 cells (the minimum depth across the 10 GoM volumes), then re-smoothed via the StructuralSmoother module at the truncated resolution so that the smoothing scale is consistent across settings. Slice planes are placed with a 10% boundary margin on each horizontal axis (to avoid boundary-layer artifacts) and an orientation split of 50% inline vs 50% crossline per setting, sampled without replacement at integer slice indices. Inline and crossline indices are drawn from independent random streams (per-model seeds 42 + model\_index and 42 + model\_index + 10000 respectively), and the SEAM volumes are extracted as 12 sub-regions of 1000  $\times$  1000 cells with 79 slices per sub-region. Before slicing, each of the 42 3D velocity volumes is normalized in place to fit  $v_p \in [1500, 5000]$  m/s: a linear rescale from  $[v_{\min}, v_{\max}]$  to  $[v_{\min}, 5000]$

Table 11: Per-stage build for the Gulf of Mexico setting. Speedup is the ratio of CPU to GPU build time. Avg / pk util are weighted-average and peak GPU utilization sampled at 10 Hz across the stage. Pk CPU memory is the maximum sampled CPU memory usage.

#	Stage	GPU s build	CPU s build	Speedup	Pk GPU memory (GB)	Avg util %	Pk util %	Pk CPU memory (GB)
1	basement	0.254	0.024	0.09x	0.04	0.0	0	0.00
2	deep_lower_tertiary	48.448	898.372	18.54x	19.89	60.4	69	20.56
3	squish_1	0.461	10.536	22.85x	7.51	5.0	5	6.64
4	mid_tertiary	34.037	702.630	20.64x	23.25	66.7	73	24.09
5	upper_miocene_pliocene	38.886	775.983	19.96x	25.27	65.5	75	25.84
6	squish_2	0.656	19.518	29.74x	18.45	0.0	0	15.15
7	lower_pliocene_basal	32.194	642.655	19.96x	28.12	68.3	81	28.93
8	lower_pliocene_upper	13.520	279.740	20.69x	28.65	66.3	72	29.18
9	squish_3	1.081	26.369	24.39x	24.49	9.0	33	20.02
10	mid_pliocene_shale	17.827	369.199	20.71x	30.80	68.8	100	31.69
11	upper_pliocene_transition	7.931	169.656	21.39x	24.37	64.9	72	25.25
12	squish_4	0.834	29.767	35.70x	29.02	28.8	64	23.42
13	upper_pliocene_reservoir	22.693	430.846	18.99x	33.10	67.4	100	33.96
14	pleistocene	8.617	181.304	21.04x	24.74	65.8	72	25.59
15	squish_5	0.900	31.409	34.89x	32.39	28.9	100	26.31
16	water	0.000	0.016	45.31x	6.87	0.0	0	0.00
17	salt_bodies	45.527	44.350	0.97x	30.32	0.7	68	19.92
18	wedging	94.578	96.718	1.02x	38.62	2.8	100	92.80
19	canonical_sos	33.502	1303.356	38.90x	52.31	97.3	100	58.67
Total		401.95	6012.45	14.96x	52.31	45.5	100	92.80

Table 12: Per-module totals over all four settings.  $n$  is the number of times each stage is invoked; *GPU s* and *CPU s* are the summed times for each stage. *Avg util* is the average GPU utilization (sampled at 10 Hz). *Peak GPU memory* is the maximum GPU memory used by the module.

Module	$n$	GPU s	CPU s	Speedup	Avg util %	Peak GPU memory (GB)
Deposit	27	773.15	10480.82	13.56×	66.7	36.92
SaltSDT	3	319.84	267.94	0.84×	0.9	30.32
SaltWedge	3	243.97	253.88	1.04×	2.7	44.53
Fault	4	240.66	9372.30	38.94×	84.6	67.67
StructuralSmoother	4	119.02	4111.62	34.55×	95.8	60.00
Deposit (drape)	1	37.12	730.08	19.67×	67.6	37.80
DeltaClinoformDeposit	1	28.22	360.27	12.77×	73.3	14.81
Squish	12	10.09	235.35	23.33×	16.4	32.39
CarbonatePlatform	2	3.59	88.35	24.63×	29.9	10.32
Basement seed	4	0.43	0.16	0.38×	0.0	0.80
Trim/clamp	2	0.29	3.65	12.74×	0.0	21.70
Water column	4	0.00	0.04	13.45×	0.0	8.99

when  $v_{\max} > 5000$  (preserving every relative velocity contrast within the volume), followed by a hard clip floor at 1500. All extracted 2D slices inherit this normalization, so the 4,276 shipped slices satisfy  $v_p \in [1500, 5000]$  m/s without further per-slice modification, consistent with the dispersion (Section E.3.1) and CFL (Section E.3.2) constraints derived below.

**Splits.** Per-setting train slice counts: F3  $10 \times 97 = 970$ , GoM  $10 \times 73 = 730$ , faulted-complex  $5 \times 145 = 725$ , salt-canopy  $4 \times 181 = 724$ , SEAM  $12 \times 79 = 947$ . The training split is the union of these slices,  $970 + 730 + 725 + 724 + 947 = 4,096$ . Twenty additional slices per training setting form a 100-slice in-distribution test split drawn from non-overlapping indices within the same volumes. The 80 Penobscot slices form the out-of-distribution test split, giving a dataset-wide total of  $4,096 + 100 + 80 = 4,276$  2D slices.

**Parquet index.** The benchmark root indexes 47,078 rows total: 42 3D models, 4,276 slices, 21,380 wavefields ( $4,276 \times 5$  frequency bands), and 21,380 shot-gather cubes. Each row carries 25 columns, including `slice_id`, `model_id`, `data_type` (model, slice, wavefield, or gather), `model_type`, `split`, `file_path`, `orientation`, `frequency_band`, source coordinates, and pre-computed per-slice velocity statistics. Slices and their paired wavefields and shot-gather cubes share

the same `slice_id`, so joining across `data_type` on `slice_id` materializes the paired triplets at any given frequency band.

## E.2 Continuous PDE and boundary conditions

The forward simulator solves the 2D acoustic, constant-density, isotropic wave equation in the  $(x, z)$  plane. With  $p(x, z, t)$  the pressure wavefield,  $v_p(x, z)$  the velocity model, and  $s(x, z, t)$  the source term (a band-limited Ricker pulse, Section E.4),

$$\frac{1}{v_p(x, z)^2} \frac{\partial^2 p}{\partial t^2} - \left( \frac{\partial^2 p}{\partial x^2} + \frac{\partial^2 p}{\partial z^2} \right) = s(x, z, t). \quad (2)$$

The factor  $1/v_p^2$  scales the temporal acceleration term: lower-velocity regions have a larger coefficient on  $\partial_t^2 p$ , so they admit slower propagation. The Laplacian  $\partial_x^2 + \partial_z^2$  measures spatial curvature of the wavefield, which is the restoring force that drives propagation.

**Initial conditions.** The pressure and its time derivative are zero everywhere at  $t = 0$ ,  $p(x, z, 0) = 0$  and  $\partial_t p(x, z, 0) = 0$ . The wavefield is excited entirely by the source term  $s$ , which fires a localized Ricker pulse near the surface (Section E.5).

**Free surface at the top.** The top edge of the simulation domain ( $z = 0$ ) is a free surface, modeling the air–water (or air–rock) interface where pressure must vanish:

$$p(x, 0, t) = 0, \quad t \in [0, T]. \quad (3)$$

This is enforced in Devito by the `fs=True` setting on the `Model` object [Louboutin et al., 2019] and produces the sign-flipped reflection of upgoing energy back into the model that is characteristic of marine acquisitions.

**Cerjan-style sponge damping on the other three sides.** The left, right, and bottom edges are absorbing rather than physical: the simulation grid is just a truncation of an unbounded earth model, and we want waves arriving at those edges to dissipate without spurious reflection. Devito’s `bcs="damp"` configuration adds a 60-cell sponge layer along each absorbing side, following the formulation of Cerjan et al. [1985]: inside the sponge, the wave equation acquires a first-order temporal-damping term proportional to a position-dependent damping coefficient  $\eta(\mathbf{x})$ ,

$$\frac{1}{v_p(\mathbf{x})^2} \frac{\partial^2 p}{\partial t^2} - \nabla^2 p + \eta(\mathbf{x}) \frac{\partial p}{\partial t} = s(\mathbf{x}, t). \quad (4)$$

The coefficient is zero throughout the interior, recovering (2) there, and rises smoothly to its peak at the outer edge. With  $n_{\text{bl}}$  damping cells,  $h$  the grid spacing, and  $\rho \in [0, 1]$  the normalized distance into the sponge,

$$\eta(\mathbf{x}) = \frac{c_{\text{damp}}}{h} \left[ \rho - \frac{\sin(2\pi\rho)}{2\pi} \right], \quad c_{\text{damp}} = \frac{1.5 \ln(1/R)}{n_{\text{bl}}}, \quad (5)$$

where  $R = 10^{-3}$  is the target reflection coefficient at the outer edge (−60 dB). The  $\sin(2\pi\rho)/(2\pi)$  term tapers the rate of growth so  $\eta$  rises gradually rather than as a hard step, which is what keeps the damping itself from generating new spurious reflections. With  $n_{\text{bl}} = 60$  and  $h = 10$  m, the sponge thickness is 0.6 km — wide enough at our highest band ( $f_{\text{max}} = 25$  Hz) for waves to traverse the layer over multiple wavelengths and so be attenuated to the design tolerance before reaching the outer boundary.

## E.3 Solving the Wave Equation Numerically

### E.3.1 Spatial Sampling (Dispersion Control)

Finite-difference schemes propagate short-wavelength components too slowly relative to the true phase velocity, an artifact known as numerical dispersion [Liu and Sen, 2009]. To keep this error below a prescribed tolerance, the grid must resolve the shortest wavelength  $\lambda_{\text{min}} = v_{\text{min}}/f_{\text{max}}$  with at least  $G$  grid points:

$$h \leq \frac{v_{\text{min}}}{G f_{\text{max}}}.$$

The required  $G$  depends on the stencil order: higher-order schemes need fewer points per wavelength for the same accuracy. For our 8th-order spatial stencil,  $G = 4$  keeps the phase-velocity dispersion error well below 1 % over the bandwidths we simulate, so the grid spacing is fixed by the highest-frequency content propagating through the slowest part of the model.

### E.3.2 CFL Stability Condition

Once  $h$  is chosen, the time step cannot be chosen independently. The Courant–Friedrichs–Lewy (CFL) condition provides the maximum  $\Delta t$  for which the explicit time-marching scheme remains stable [Courant et al., 1928]:

$$\Delta t \leq \sigma_{\max} \frac{h}{v_{\max}},$$

where  $\sigma_{\max} = \left( \sqrt{d \sum_{m=1}^M |a_m|} \right)^{-1}$  is the maximum stable Courant number,  $d$  is the number of spatial dimensions, and  $\{a_m\}_{m=1}^M$  are the finite-difference coefficients [Fornberg, 1988]. Note the asymmetry: the dispersion criterion involves  $v_{\min}$  (shortest wavelength), while stability involves  $v_{\max}$  (fastest propagation). Both constrain us simultaneously.

### E.3.3 Temporal Subsampling (Nyquist)

The CFL bound forces  $\Delta t = 1$  ms for stability, but the band-limited wavefield does not need to be saved at that rate. Storing every computational step would inflate the dataset by an order of magnitude without adding any information that the band-limit cannot already recover, and would slow training throughput in proportion. Shannon–Nyquist sets the floor: a signal band-limited at  $f_{\max}$  can be reconstructed exactly from samples taken every  $1/(2f_{\max})$  seconds. We therefore save every  $k$ -th computed step, where

$$k = \left\lfloor \frac{N}{2f_{\max}T} \right\rfloor.$$

This yields  $N_{\text{saved}} = \lceil N/k \rceil$  snapshots at an effective sampling interval of  $\Delta t_{\text{saved}} = k \cdot \Delta t$ . We use  $k = 14$  uniformly across all five frequency bands so the saved tensor has the same temporal dimension regardless of source bandwidth; this is conservative for the lower bands (Table 14) but yields a uniform  $(N_{\text{saved}}, n_z, n_x)$  shape that batches naturally during training.

### E.3.4 Configuration Summary

The central design constraint is that every simulation, regardless of which frequency band the source wavelet targets, must produce a wavefield tensor of identical shape. Neural operators expect fixed-size inputs during training, and batching requires uniform dimensions. We therefore adopt a single spatial grid, a single time step, and a single temporal subsampling factor across all 21,380 wavefield simulations and 21,380 shot-gather cube simulations (5 frequency bands  $\times$  4,276 slices); Table 13 summarizes the resulting simulation parameters.

Here  $M$  is the spatial half-stencil width: the number of grid points on each side of the central node used to approximate the second spatial derivative. An 8th-order scheme ( $M = 4$ ) reaches four neighbors in each direction, a common choice that balances accuracy against computational cost.

**Absorbing boundary and slice margin.** Each simulation grid is padded on its left, right, and bottom with a 60-cell sponge damping zone ((4), (5)); the top edge is a free surface (3). The slice extraction step (Section E.1) reserves a 10 % lateral margin from each cube edge, and source positions reserve an additional 0.5 km margin inside the absorbing-boundary region during forward modeling, so sources radiate into the physical interior rather than into the damping layer.

We generated the wavefields and shot-gather cubes for each of the five frequency bands. The bands differ only in the source wavelet, so the grid, time step, and saved tensor shape are identical across all bands. The Nyquist margin in Table 14 is the ratio of the highest frequency the saved sampling can faithfully represent ( $1/(2\Delta t_{\text{saved}}) \approx 35.7$  Hz at  $\Delta t_{\text{saved}} = 14$  ms) to the band’s upper cutoff  $f_{\max}$ . A margin of  $1 \times$  would put  $f_{\max}$  exactly at the Nyquist limit; values larger than  $1 \times$  mean the band is oversampled and aliasing-free at the saved rate. We chose  $\Delta t_{\text{saved}} = 14$  ms so that all five bands clear Nyquist with a margin of at least  $\sim 1.4 \times$ .

Table 13: Simulation parameters shared across all 5 frequency bands. Wavefields and shot-gather cubes share the same grid, time step, stencil order, boundary, and subsampling factor; they differ only in recording time, source geometry, and whether the full wavefield or a receiver-extracted gather is saved.

Parameter	Symbol	Value
Grid spacing	$h$	10 m (isotropic)
Spatial FD order	$2M$	8 ( $M = 4$ )
Max P-wave velocity	$v_{\max}$	5000 m/s
Min P-wave velocity	$v_{\min}$	1500 m/s
Computational time step	$\Delta t$	1.0 ms
Recording time (wavefield)	$T$	5.0 s
Recording time (shot-gather)	$T$	8.0 s
Total computational steps	$N$	5001 (wavefield) / 8001 (gather)
Subsampling factor	$k$	14
Saved snapshots (wavefield)	$N_{\text{saved}}$	358
Saved time samples (gather)	$N_{\text{saved}}$	572
Saved time interval	$\Delta t_{\text{saved}}$	14.0 ms
Slice depth	$n_z$	619
Slice width	$n_x$	1000 (typical)
Source wavelet	—	Bandpass Ricker (Section E.4)
Absorbing boundary	—	60-cell sponge damping; free top
<b>Wavefield tensor shape</b>	—	<b>(358, 619, 1000)</b>
<b>Shot-gather cube shape</b>	—	<b>(64, 572, 1000)</b>

Table 14: Frequency bands for wavefield and shot-gather generation. Nyquist margin =  $1/(2f_{\max}\Delta t_{\text{saved}})$  at  $\Delta t_{\text{saved}} = 14$  ms, i.e., the factor by which each band’s upper cutoff falls below the saved-sampling Nyquist limit of 35.7 Hz. We use only the 3–6 Hz band for the wavefield prediction experiments in Section 5; all five bands are released on the Hugging Face dataset.

Band	Frequency range	$f_{\max}$ (Hz)	Nyquist margin
1	3–6 Hz	6	$5.95\times$
2	3–8.5 Hz	8.5	$4.20\times$
3	3–12 Hz	12	$2.98\times$
4	3–17.5 Hz	17.5	$2.04\times$
5	3–25 Hz	25	$1.43\times$

#### E.4 Source Wavelet

The source time function is a Ricker pulse with peak frequency  $f_0$ , then bandpass-filtered with a 4th-order zero-phase Butterworth (forward-backward filtering via `scipy.signal.sosfiltfilt`) at the band corners listed in Table 14. The peak frequencies are  $f_0 \in \{4.50, 5.75, 7.50, 10.25, 14.00\}$  Hz for the five bands respectively, and each wavelet is centered at  $t_0 = 1/f_0$ .

After filtering, the amplitude of the wavelet depends sensitively on the passband, so we apply a two-step normalization for numerical stability and physical scaling. We first divide by the  $\ell_2$  norm of the filtered signal, which puts every band’s wavelet on the same numerical footing. We then multiply by  $\sqrt{B/24}$  Hz, where  $B$  is the band’s bandwidth and 24 Hz is a fixed reference bandwidth chosen to match a typical broadband seismic source (e.g. a 2–26 Hz band). This  $\sqrt{B}$  scaling restores the Parseval relationship between bandwidth and energy: a band-limited signal’s radiated energy is proportional to its passband width, so wider-band sources radiate more energy than narrower-band sources, matching what a real source array does. Without this rescaling, unit-energy normalization alone would make all five bands radiate the same total energy, which is not physical.

#### E.5 Wavefield and shot-gather acquisition geometry

All simulations are run in Devito [Louboutin et al., 2019], a SymPy-based domain-specific language that JIT-compiles vectorized OpenMP-parallel C from finite-difference stencils. Two acquisition

configurations are used, sharing the same grid, time step, and absorbing boundary but differing in source count, receiver geometry, and recording time.

**Wavefield generation (5 s, single source, no receivers).** For each (slice, band) pair we run one 5 s acoustic simulation with a single source placed at depth 10 m and a uniformly random horizontal position drawn from the lateral interval  $[1.1 \text{ km}, x_{\max} - 1.1 \text{ km}]$ . The 1.1 km margin excludes the 60-cell sponge (0.6 km) plus a 0.5 km surveying buffer on each side, so the source pulse propagates entirely inside the physical domain rather than into the damping zone. Per-slice randomization is reproducible: the seed is  $42 \oplus \text{CRC32}(\text{slice filename})$ . We save the full wavefield  $p(\mathbf{x}, t)$  subsampled in time by  $k = 14$ , producing one tensor per (slice, band) of shape  $(358, n_x, 619)$ . With 4,276 slices and 5 bands, this gives 21,380 wavefield tensors in total.

**Shot-gather generation (8 s, 64 sources, 1000 receivers).** For each (slice, band) pair we run one 8 s simulation that emulates a marine streamer survey. 64 source positions are uniformly spaced across the same valid lateral interval at depth 10 m, and 1000 receivers at depth 10 m are uniformly spaced across the full lateral extent. The receiver array is fixed in place (common-receiver streamer geometry): the same 1000 receivers record all 64 source firings, rather than a streamer that translates with the source. The output cube has shape  $(64, 572, 1000) = (\text{sources}, \text{time}, \text{receivers})$ , where 572 is the number of saved time samples after  $k = 14$  subsampling of the 8001 computational steps. We use 8 s rather than 5 s here so the deepest reflections from the 6.19 km depth column have time to return to the surface ( $2 \cdot 6.19 \text{ km} / v_{\text{shallow}} \approx 8 \text{ s}$  with  $v_{\text{shallow}} \approx 1500 \text{ m/s}$  in the water layer). Fig. 11 shows representative cubes from three training settings.

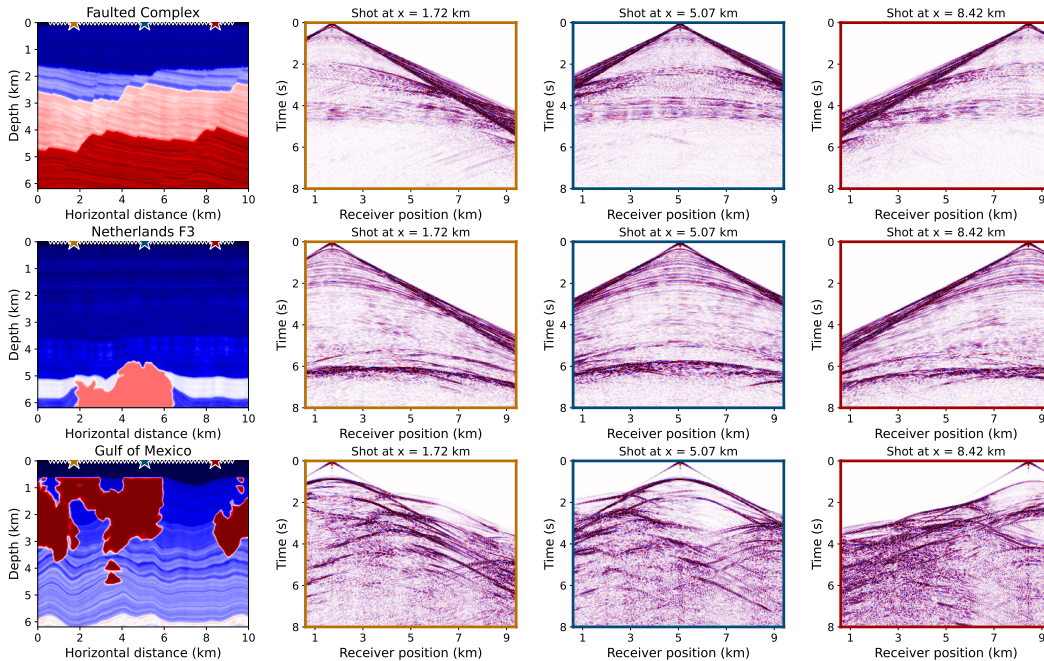


Figure 11: Representative 8 s shot gathers from three training settings: Fault (top row), F3 (middle row), and GoM (bottom row). For each setting, the gathers correspond to three near-surface source positions on the left, center, and right of the lateral extent, color-coded to indicate source location.

## F Wavefield Prediction

This appendix gives architecture, rollout, loss, training, and evaluation details for the wavefield-prediction experiments of Section 5. The task is to predict the wavefield (5 s of acoustic propagation at 3–6 Hz) given the velocity slice and a binary source mask; we evaluate three operators: TFNO

(chunked autoregressive forward prediction), TFNO-interp (anchor-bounded interior prediction), and DPOT (transformer with adaptive Fourier mixing).

## F.1 Task setup and preprocessing

**Tensor shapes.** Each chunked-rollout example has input shape  $(C_{\text{in}}, H, W) = (12, 619, 1000)$  where  $C_{\text{in}} = T_{\text{in}} + 2$  stacks the 10 wavefield seed frames, the velocity slice, and the binary source mask. The per-chunk target has shape  $(T_{\text{out}}, H, W) = (50, 619, 1000)$ . The full forward-modeled trajectory has 358 saved snapshots; the first 10 form the seed window, leaving 348 frames to predict, so the inference-time rollout chains  $\lceil 348/50 \rceil = 7$  chunks. The seventh chunk’s leading 48 frames are kept and its trailing 2 are discarded.

**Normalization.** Wavefield amplitudes vary by orders of magnitude across samples (different source positions, velocity contrasts, recording windows), so each sample is normalized by its own peak input amplitude:

$$s = \max_{t,y,x} |x_{\text{wf}}(t, y, x)|, \quad \tilde{x}_{\text{wf}} = x_{\text{wf}}/s, \quad \tilde{y} = y/s.$$

The same scale  $s$  is applied to the target so the model learns a unit-amplitude mapping. At inference time the prediction is rescaled by  $s$  to recover absolute amplitudes. Velocities use a global min–max to  $[0, 1]$  over  $[v_{\text{min}}, v_{\text{max}}] = [1500, 5000]$  m/s; the source mask is already binary and is passed through unchanged.

## F.2 Architectures

The three operators we compare are TFNO, TFNO-interp, and DPOT. TFNO and TFNO-interp share the same channel-projection layout following Zhang et al. [2023]: a  $1 \times 1$  convolution Dp1 compresses the  $C_{\text{in}}$  input channels to a latent width  $d_w$ , the backbone operates on  $(d_w, H, W)$ , and a  $1 \times 1$  convolution Dp2 expands the latent representation to the per-chunk output channel count. DPOT does not use external Dp1/Dp2 layers; its patch embedding compresses the  $C_{\text{in}}$  input channels directly into the embedding space, and an unpatchify head produces the output frames.

**TFNO.** The Tucker-factorized Fourier Neural Operator [Li et al., 2021, Kossaifi et al., 2024] replaces the dense complex spectral weight tensor with a Tucker decomposition at rank fraction 0.5, reducing the spectral parameter count by  $\sim 4\times$  at the same width. The backbone configuration: 4 layers, `n_modes` = (32, 64), `hidden_channels` = 48,  $d_w = 40$ , GELU activations, linear FNO skips, soft-gating channel-MLP skip connections, grid positional embedding, and 5% per-side zero-padding on the spatial domain to break the FFT’s implicit periodic boundary (without padding the absorbing-boundary energy at the bottom of the volume wraps to the free surface). The  $T_{\text{out}} = 50$  output channels of Dp2 produce one chunk per forward pass.

**TFNO-interp.** The interp variant uses the same TFNO2d backbone hyperparameters as TFNO but wraps it in a `BoundaryAnchoredInterpPredictor`: instead of forward prediction past a single seed window, it fills a  $\tau = 20$  frame interior gap between two stored 20-frame anchor windows ( $T_L = T_R = 20$ ). The wrapper predicts a  $\tau$ -frame residual via a sine-windowed head:

$$\hat{u}(t) = (1 - \alpha_t) u_{\text{anchor end}} + \alpha_t u_{\text{anchor start}} + \sin(\pi\alpha_t) r_\theta(t), \quad \alpha_t = \frac{t+1}{\tau+1},$$

where the linear-in- $\alpha_t$  part interpolates between the anchor frames,  $r_\theta(t)$  is the network output, and the sine envelope  $\sin(\pi\alpha_t)$  forces the prediction to match the anchor frames exactly at the gap endpoints ( $\alpha_t = 0, 1$ ) while peaking in the middle of the gap.

**DPOT.** DPOT [Hao et al., 2024] is a ViT-style operator with patch embedding, AFNO (Adaptive Fourier) mixing, and learned positional information. We use the `DPOTAdapterSimple` configuration with embedding dimension 256, 4 transformer blocks, `num_blocks` = 4 (block-diagonal AFNO structure), `modes` = 16 (AFNO frequency truncation), MLP ratio 1.0, patch size 8, and GELU activations. As noted above, DPOT projects the  $C_{\text{in}}$  input channels into the embedding space through its patch embedding rather than through external  $1 \times 1$  convolutions, and an unpatchify head produces the  $T_{\text{out}}$  output frames.

### F.3 Hybrid (chunked autoregressive) rollout

The full forward-modeled trajectory has 358 saved snapshots (Section E); the model only predicts  $T_{\text{out}} = 50$  at once. Autoregressive chaining is the operator-learning analogue of how a standard finite-difference solver advances from the  $t = 0$  initial condition to all subsequent times: each chunk uses the model’s previous output as its next initial condition, so the same single trained operator generates the full trajectory rather than a separate model per horizon. Two extreme rollout strategies are unattractive: single-step ( $T_{\text{out}} = 1$ ) autoregression accumulates error over 348 steps and is known to compound to large drift in long horizons; full-trajectory ( $T_{\text{out}} = 348$ ) prediction in one forward pass would inflate the output channel count by  $\sim 7\times$  relative to our chunk size, exceeding the activation budget at the field-scale grid of (619, 1000) on a single A100. We instead use a chunked autoregressive rollout (Algorithm 9): the model produces  $T_{\text{out}}$  frames per pass, the last  $T_{\text{in}}$  predicted frames seed the next pass, and per-chunk amplitude renormalization mirrors the per-sample normalization used during training. With  $T_{\text{out}} = 50$  and 348 frames to predict,  $\lceil 348/50 \rceil = 7$  chunks suffice; only the leading 48 frames of the seventh chunk are retained (the trailing 2 fall past the end of the saved trajectory and are discarded).

---

**Algorithm 9** autoregressive\_rollout — chunked wavefield prediction.

---

**Require:** Trained model  $M$ ; seed  $u_{0:T_{\text{in}}}$ ; velocity  $v$ ; source mask  $m$ ; total length  $T$ ; chunk size  $T_{\text{out}}$ ; bounds  $v_{\text{min}}, v_{\text{max}}$ .

**Ensure:** Predicted wavefield  $\hat{u}_{T_{\text{in}}:T}$ .

- 1: Normalize velocity once:  $\tilde{v} \leftarrow (v - v_{\text{min}})/(v_{\text{max}} - v_{\text{min}})$ .
- 2: Buffer  $b \leftarrow u_{0:T_{\text{in}}}$  (sliding window of last  $T_{\text{in}}$  frames).
- 3: **for**  $k = 0, 1, \dots, \lceil (T - T_{\text{in}})/T_{\text{out}} \rceil - 1$  **do**
- 4:    $s \leftarrow \max |b|$ ;  $\tilde{b} \leftarrow b/s$ . ▷ per-chunk amplitude scale
- 5:    $x \leftarrow [\tilde{b}, \tilde{v}, m]$  stacked on the channel axis.
- 6:    $\hat{u}_{\text{chunk}} \leftarrow s \cdot M(x)$ . ▷ denormalize the prediction
- 7:   Append the needed prefix of  $\hat{u}_{\text{chunk}}$  to the output.
- 8:   Update  $b$ : take the last  $T_{\text{in}}$  frames of  $\hat{u}_{\text{chunk}}$  (or slide if  $T_{\text{out}} < T_{\text{in}}$ ).
- 9: **end for**

---

### F.4 Loss

Training minimizes a temporally-weighted relative  $L^2$  loss:

$$\mathcal{L} = \mathbb{E}_{\text{batch}} \left[ \sqrt{\frac{\sum_t w(t) \|\hat{u}_t - u_t\|_2^2}{\sum_t w(t) \|u_t\|_2^2 + \varepsilon}} \right].$$

The temporal weight schedule  $w(t)$  is motivated by error compounding in autoregressive rollouts: errors in the first few predicted frames seed the input buffer for the next chunk and propagate forward, so accuracy at small  $t$  has higher leverage on long-horizon stability than accuracy at large  $t$ . Coker et al. [2025] formulate the same hypothesis for autoregressive neural operators on 1D PDEs (“giving higher priority to earlier timesteps will reduce the overall propagation of errors and enhance training stability”). Our schedule applies the practice statically:  $w(t)$  decays linearly from  $w_{\text{start}} = 1.0$  at  $t = 0$  to  $w_{\text{end}} = 0.5$  at  $t = T_{\text{out}} - 1$ , scaling the gradient signal in proportion to that leverage.

TFNO and DPOT use the linear temporal weighting just described. TFNO-interp uses uniform temporal weighting ( $w_{\text{start}} = w_{\text{end}} = 1.0$ ) because its prediction is bounded symmetrically by anchor frames at both endpoints — there is no early-vs-late asymmetry to exploit — plus an additional first-difference temporal-derivative term, weight  $\alpha_{\text{dt}} = 0.1$ , that penalizes  $\|\partial_t(\hat{u} - u)\|_2^2$  across the gap.

### F.5 Training configuration

As shown in Table 15, the one training-hyperparameter deviation across architectures is the base learning rate: in preliminary short runs DPOT exhibited substantially larger batch-level oscillations in training loss at  $2 \times 10^{-3}$ , so we lowered DPOT’s base LR to  $5 \times 10^{-4}$  with the same cosine decay. The adjustment is consistent with the original DPOT recipe [Hao et al., 2024], which uses AdamW

Table 15: Wavefield prediction training hyperparameters per architecture. The three runs share the same optimizer, schedule shape, weight decay, gradient clipping, mixed-precision policy, batch size, and epoch count, so the comparison is on architecture rather than training hyperparameters. The one deviation is the base learning rate (see text).

	TFNO	TFNO-interp	DPOT
Optimizer	AdamW	AdamW	AdamW
Learning rate	2e-3	2e-3	5e-4
Weight decay	1e-4	1e-4	1e-4
Schedule	cosine	cosine	cosine
Min LR (cosine floor)	1e-5	1e-5	1e-5
Gradient clip ( $\ell_2$ )	1.0	1.0	1.0
Mixed precision	yes	yes	yes
Per-GPU batch	8	8	8
Grad-accumulation steps	4	4	4
Effective batch	64	64	64
Epochs	10	10	10
$w_{\text{start}}, w_{\text{end}}$	1.0, 0.5	1.0, 1.0	1.0, 0.5
$\alpha_{\text{dt}}$	0.0	0.1	0.0

with a one-cycle schedule and a long warmup phase, implying a much smaller effective learning rate at the onset of training; using a smaller cosine peak LR for DPOT mirrors that effect within our cosine-only schedule.

All three runs are trained on  $2 \times$  NVIDIA A100 80 GB via DDP, with effective batch 64 ( $8 \times 4$  grad-accum steps  $\times 2$  GPUs). We decompress the source HDF5 files to NPY files during preprocessing and use the NPY files for training, which allows us to avoid the decompression overhead of HDF5. All reported runs use a single seed. Each run takes about 24 hours.

## F.6 Evaluation pipeline and reported metrics

We evaluate trained operators on the in-distribution test set (100 slices, five training settings with non-overlapping indices) and the out-of-distribution test set (80 Penobscot slices). For each (operator, slice) pair we run a forward rollout from the seed window, compute per-sample per-frame and per-wavenumber metrics, write the per-sample numbers into a parquet manifest, and aggregate across the test set to produce the figures reported in Section 5.

The metrics computed per sample are: relative  $L^2$  error per frame  $L_{\text{RE}}^2(t) = \|\hat{u}_t - u_t\|_2 / (\|u_t\|_2 + \epsilon)$  (plotted on the log-y “L2RE” axis of Fig. 6 as a per-frame mean across the test set, on a physical-time axis, with in-distribution and out-of-distribution test splits side-by-side); a per-wavenumber relative power-spectrum error  $|P_{\text{pred}}(k) - P_{\text{gt}}(k)| / (P_{\text{gt}}(k) + \epsilon)$ , where  $P(k)$  is the azimuthally-averaged radial 2D power spectrum first averaged over the trajectory’s frames (this is *not* a vector  $L^2$  norm; it is plotted as “Relative spectral error” in Fig. 12); trajectory-wide rel- $L^2$ ; max-absolute-error; energy ratio  $E[-1]/E[0]$  and per-frame energy std; divergence time (first frame where  $\|\hat{u}\|_\infty > 10 \|u\|_\infty$  or NaN/Inf); per-frame SSIM; and a physics-residual ratio computed from the discretized acoustic wave operator.

The signed-error panel grids show  $\hat{u} - u$  at four selected frames on a shared symmetric color scale, with a velocity-grayscale backdrop ( $\alpha = 0.3$ ) and a star marking the source position. The chunked-rollout panel (Fig. 4) is a one-shot teacher-forced chunk seeded from GT frames [240, 250) and predicting frames [250, 300) at sampled positions 256, 270, 285, 299 (no autoregressive chaining for this figure). The TFNO-interp panel (Fig. 5) shows signed error at gap centers (frames 30, 150, 230, 270) of the stitched rollout; its colorbar reuses Fig. 4’s clim so error magnitudes are directly comparable across the two protocols. Fig. 6 additionally shades TFNO-interp’s gap-prediction windows in light gray and diagonally hatches the trailing window past the last anchor (frames 340–358, equivalently 4.76–5.00 s, which the model does not predict).

Each metric tells us a different thing: the per-frame rel- $L^2$  curve shows how prediction error compounds (or stays bounded) as the rollout extends; the spectral curve isolates the failure mode of neural operators at high wavenumbers, the spectral-bias regime; the energy ratio diagnoses whether the rollout is dissipating or blowing up; divergence time picks out catastrophic failures; and the

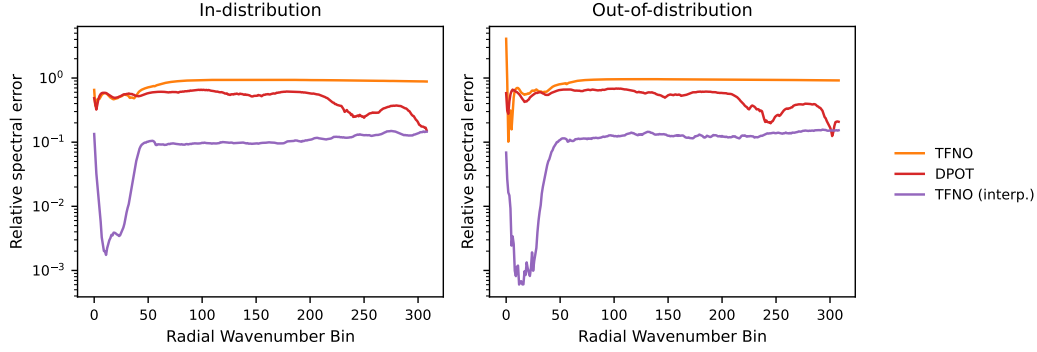


Figure 12: Per-wavenumber relative spectral error on the in-distribution (left) and out-of-distribution (right) test sets. TFNO-interp dominates across the spectrum; DPOT outperforms TFNO at high wavenumbers.

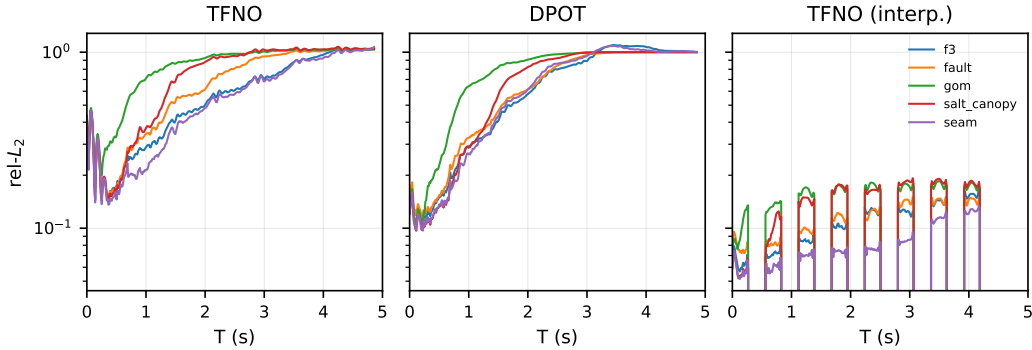


Figure 13: L2RE versus time for each geological setting in the in-distribution test set. Gulf of Mexico and Salt Canopy are the most challenging settings, while SEAM and F3 are the easiest.

physics-residual ratio measures how well the prediction satisfies the governing PDE without referring to the ground truth.

## E.7 Per-wavenumber and per-geology breakdowns

**Per-wavenumber error.** Fig. 12 plots the per-wavenumber relative power-spectrum error. TFNO-interp dominates across the spectrum; DPOT outperforms TFNO at high wavenumbers.

**Per-geology error.** Fig. 13 displays the L2RE per geological setting in the in-distribution test set. Across all architectures, the Gulf of Mexico and Salt Canopy settings are the most challenging, while SEAM and F3 are the easiest. We suspect this is due to Gulf of Mexico and Salt Canopy being the most salt-rich settings in the dataset.

## G End-to-End Seismic Inversion

This appendix gives architecture, loss, and training details for the end-to-end encoder–decoder inversion experiments of Section 6. The task is to map a 3D shot-gather cube (produced by 8 s of acoustic propagation at 3–25 Hz) to a 2D  $v_p(\mathbf{x})$  velocity model.

## G.1 Task setup and preprocessing

**Tensor shapes.** The input is a 3D shot-gather cube of shape  $(n_{\text{shots}}, n_{\text{time}}, n_{\text{receivers}}) = (64, 572, 1000)$ , presented to the network as  $(B, 1, 64, 572, 1000)$ , where  $B$  is the batchsize. The output is a 2D velocity slice of shape  $(B, 1, 619, 1000)$  in the normalized velocity range  $[0, 1]$ .

**Normalization.** Shot gathers are normalized by sign-preserving clipping. We compute a single global clipping threshold once during preprocessing. We randomly sample 200 training shot-gather cubes, take the 98th percentile of the absolute amplitudes within each cube, then take the 98th percentile of those per-cube values to obtain the global threshold. At training time, every shot-gather cube has its amplitudes clipped at plus or minus this threshold and divided by the threshold, mapping values to  $[-1, 1]$ . Velocities are mapped to  $[0, 1]$  by an affine transformation that sends 1500 m/s to 0 and 5000 m/s to 1.

**Augmentation.** During training, the (shot-gather cube, velocity slice) pairs are augmented with a horizontal flip (probability 0.5, applied jointly to the receiver axis of the cube and the horizontal axis of the velocity slice so their relationship through the acoustic wave equation (1) is preserved) and additive Gaussian noise with signal-to-noise ratio drawn uniformly between  $[10, 30]$  dB.

## G.2 Architectures

We compare three encoder–decoder architectures. The Transformer and CNN encoders share an identical architecture for the decoder. InversionNet is used because it has been employed in OpenFWI [Deng et al., 2022].

**InversionNet.** A direct port of the 2D encoder–decoder of Wu and Lin [2020]. The shot-gather cube is treated as a 2D image with 64 channels (one per shot) and processed by a convolutional encoder followed by a deconvolution (a.k.a. transposed convolution) decoder, with a final resampling to the  $(619, 1000)$  output grid.

**3D residual CNN encoder + 2D decoder.** A 3D residual encoder following nnU-Net ResEnc principles [Isensee et al., 2024]. The first encoder stage uses an asymmetric stride that aggressively downsamples the receiver axis while preserving the shot axis; remaining stages use symmetric strides. A 3D-to-2D transition then collapses the shot dimension to produce a 2D feature map, which is fed to a 2D residual decoder that lifts the feature map back to the  $(619, 1000)$  output grid and applies a sigmoid to yield a single normalized velocity channel.

**3D Swin encoder + 2D decoder.** A small CNN stem performs spatial downsampling of the cube. A 3D patch embedding then maps the result to a token grid that is processed by a 3D Swin encoder [Liu et al., 2021, Hatamizadeh et al., 2022] via windowed self-attention with shifted-window blocks and patch merging between stages. The output of the encoder is collapsed to a 2D feature map and fed to the same decoder architecture used by the CNN architecture.

## G.3 Loss

Training minimizes the mean squared error between the predicted and ground-truth normalized velocity slices, averaged over the training set and the height and width of each slice:

$$\mathcal{L} = \frac{1}{N H W} \sum_{n=1}^N \sum_{i=1}^H \sum_{j=1}^W (\hat{v}_{n,i,j} - v_{n,i,j})^2,$$

where  $N$  is the number of training pairs,  $H = 619$  and  $W = 1000$  are the height and width of the velocity slice,  $v_{n,i,j} \in [0, 1]$  is the normalized ground-truth velocity at pixel  $(i, j)$  of the  $n$ th training sample, and  $\hat{v}_{n,i,j} \in [0, 1]$  is the corresponding model prediction.

## G.4 Training configuration

We list training hyperparameters per architecture in Table 16. All three architectures train on  $2 \times$  NVIDIA A100 80 GB via PyTorch DDP, with effective batchsize 16 ( $8 \times 1$  grad-accum steps  $\times 2$

Table 16: Inversion training hyperparameters per architecture (3–25 Hz frequency band, 8 s propagation). All three architectures share the same optimizer, schedule, and augmentation.

	InversionNet	CNN	Swin
Optimizer	AdamW	AdamW	AdamW
Learning rate	1e-4	1e-4	1e-4
Weight decay	1e-4	1e-4	1e-4
Schedule	cosine	cosine	cosine
Min LR (cosine floor)	1e-6	1e-6	1e-6
Gradient clip ( $\ell_2$ )	1.0	1.0	1.0
Mixed precision	yes	yes	yes
Per-GPU batchsize	8	8	8
Grad-accumulation steps	1	1	1
Effective batchsize	16	16	16
Epochs	100	100	100
Horizontal flip ( $p$ )	0.5	0.5	0.5
Noise injection range (dB)	[10, 30]	[10, 30]	[10, 30]

GPUs). We train three random seeds per architecture and report mean RMSE and SSIM in the main text. We decompress the source HDF5 files to NPY files during preprocessing and use the NPY files for training, which allows us to avoid the decompression overhead of HDF5. Each training run takes about 20 hours.